Determination of microphysical properties of cloud and drizzle droplets based on observations with radar, microwave radiometer, and lidar

MASTER THESIS

by
Lukas Pfitzenmaier

A thesis submitted
in partial fulfillment of the requirements
for the degree of

Master of Science (Meteorology)

at the Faculty of Physics and Earth Sciences
of the University of Leipzig

Leipzig, 12 October 2012

Reviewed by
Jun. Prof. Dr. Bernhard Pospichal
Leipzig Institute for Meteorology, Leipzig
and
Dr. habil. Albert Ansmann
Leibniz Institute for Tropospheric Research, Leipzig

Contents

1 Introduction

The relationship between air pollution, cloud properties, and climate change involves some of the currently least understood atmospheric processes. It thus attracts increasing concern within the scientific community. Aerosol particles of both natural and anthropogenic sources have been identified to play an important role for the radiation budget of the Earth atmosphere. On the one hand, aerosol particles have a direct effect on the radiation budget because they scatter and absorb incoming solar radiation as well as outgoing terrestrial longwave radiation [*Bohren and Huffman*, 1983]. On the other hand, the indirect aerosol effect is related to the influence of aerosol particles on cloud evolution that affects cloud albedo [*Twomey*, 1977], cloud life time [*Albrecht*, 1989], and the formation of precipitation [*Pincus and Baker*, 1994]. All these processes again have an influence on the radiation budget of the Earth [*Heintzenberg and Charlson*, 2009].

To quantify the direct and indirect aerosol effect the vertical and horizontal distribution of aerosol, cloud, and precipitation properties must be characterized. Knowing more about aerosols and clouds, as well as their interaction will help to minimize uncertainties in weather forecast and climate modelling [*Solomon et al.*, 2007].

Airborne or ground-based in-situ measurements are possible approaches to characterize cloud and aerosol microphysical properties and their relationship. However, airborne observations (e.g., *Miles et al.* [2000]) are limited to short time periods whereas aerosol or cloud properties measured at the ground, e.g., on mountain stations (e.g., *Richardson et al.* [2007]), are subject to surface effects that would not affect clouds in the free atmosphere. An approach to observe aerosol-cloud interaction over long time periods are remote-sensing applications. Remote sensing of cloud and aerosol microphysical properties is a subject to uncertainties, but instruments improve and so the accuracy of the measured parameters. Also combinations of instruments provide more or additional information [*Illingworth et al.*, 2007].

Based on satellite observations *Ackerman et al.* [2000] provided evidence that soot from forest fires can affect cloud formation on a regional scale. *Feingold et al.* [2003] were able to identify the cloud albedo effect (Twomey effect) from long-term ground-based remote sensing measurements. They used cloud radar (Radio Detection and Ranging) measurement to estimate the cloud-droplet effective radius [*Frisch et al.*, 1995, 1998] and related this quantity to lidar-derived (Lidar: LIght Detection And Ranging) aerosol microphysics [*Weitkamp*, 2005].

In order to investigate cloud and aerosol microphysical properties and their interaction, the Leibniz Institute for Tropospheric Research (TROPOS), Leipzig, Germany (51.3° N, 12.4° E, 125 m above sea level) performs measurements of chemical and physical processes in the atmosphere since 1992. Thereby, TROPOS relies on both in situ measurements (e.g., *Ditas et al.* [2012]) and remote sensing (e.g.,

Ansmann et al. [2005]).

Aerosol remote sensing at TROPOS is performed with lidar. Lidars operate at wavelengths in the μm-range where the sensitivity for the detection of aerosol particles is highest. With lidar it is possible to measure vertical profiles of aerosol distribution, aerosol optical properties, and the vertical motion of aerosol particles in the free atmosphere.

The radar technique is used to detect vertical profiles of clouds throughout the troposphere. For this purpose the instrument emits pulses of electromagnetic radiation with a wavelength in the mm- to the cm-range vertically into the atmosphere, and receives the power backscattered by hydrometeors. Such measurements provide profiles of the cloud radiative and microphysical properties as well of the vertical motion of the hydrometeors.

Microwave radiometer measurements at TROPOS are performed as well. The passive detection technique of the microwave radiation in regions of absorbtion lines of the microwave spectrum allows the detection of atmospheric state parameters, such as temperature and humidity, and cloud liquid water path.

The multitude of instruments available at TROPOS allows ground-based detection of aerosols, clouds, and their interaction at the same time. In the framework of this master's thesis, a method for the retrieval of cloud and drizzle microphysical properties was implemented. The thesis is based on cloud-radar measurements. Using cloud-radar data the microphysical properties of cloud droplets and drizzle droplets are determined following the approach presented in *Frisch et al.* [1995]. Further aspects of the thesis are the determination of the applicability of the implemented Frisch-method and its agreement to similar existing approaches. It will also be tested if the vertical-velocity measurement of the radar, that is needed for the retrieval of drizzle microphysics, can be improved by taking Doppler lidar measurements into account.

Chapter 2 gives an introduction to the radar theory. A short overview on the instruments and their data products used in this thesis as well as a measurement example are presented in Chapter 3. In Chapter 4 the theoretical background provided in Chapter 2 is applied to relate microphysical cloud properties to the corresponding radar signals. The two methods of *Frisch et al.* [1995] and *O'Connor et al.* [2005] used in this thesis to retrieve cloud and drizzle microphysical properties from radar measurements are introduced in Chapter 5. In Chapter 6 the cloud and drizzle microphysics as obtained after *Frisch et al.* [1995] are presented by means of two case studies. The results are compared to drizzle microphysics independently derived after *O'Connor et al.* [2005]. In Chapter 7 the same calculations are performed for a data set that was corrected for atmospheric vertical motions which may influence radar-derived fall velocities of cloud hydrometeors. A summary of the thesis as well as conclusions are given in Chapter 8.

2 Cloud radar

Radar is an acronym for Radio Detection And Ranging. It is an active remote sensing technique. By means of this method electromagnetic waves are emitted into the atmosphere via an antenna. The fraction of the radiation that is scattered back by particles gives information about hydrometeors in the detected air mass. From the time delay between emittance of the radiation and the detection of the backscattered fraction, the range at which the scattering event occurred can be determined. The following chapter gives the theoretical background of the cloud radar technique.

2.1 The difference in cloud detection between lidar and radar

Range-resolved remote sensing of clouds can be done with lidar or radar. Even though the measurement principles of both instruments equal, differences in the observed atmospheric properties arise from the differences in the wavelength of the electromagnetic radiation used by the two instruments.

The advantage of cloud detection by radar instead of lidar results from the difference in the measurement sensitivity of the instruments. Figure 1 shows the backscatter efficiency of a lidar instrument (blue curve) and of a radar instrument (grey and black curves) as a function of particle diameter. The sensitivity curve of the lidar

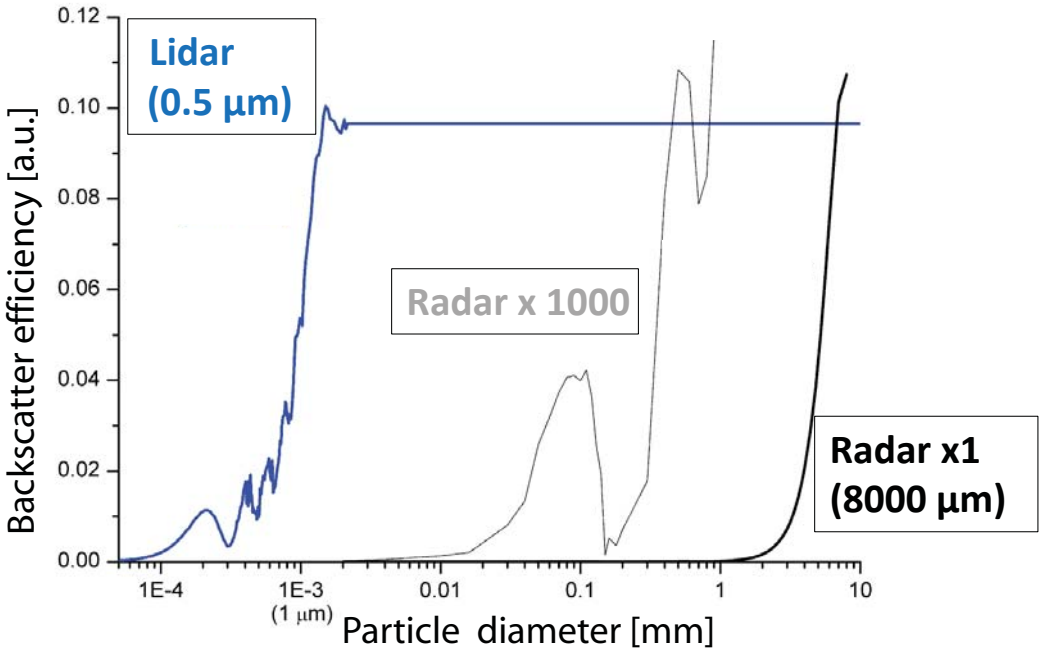

Figure 1: Lidar (blue curve) and radar (black curve) sensitivity in arbitrary units [a.u.] as a function of particle diameter. The gray curve shows the radar sensitivity scaled by a factor of 1000 (*Courtesy: U. Görsdorf*).

shows that the signal is size-dependent up to a particle diameter of 1 μm. In this size region the backscattering efficiency can be described by Rayleigh-scattering theory when the particle diameter is much smaller than the wavelength, and by Mie-scattering theory for particles with sizes similar to the wavelength [*Hansen and Travis*, 1974]. For particles larger than 1 μm the backscatter efficiency is high and independent of particle size. Particles of that size range thus quickly attenuate the radiation of a wavelength of 500 nm. In this size range that is much larger than the wavelength, geometrical-scattering theory must by applied [*Hansen and Travis*, 1974].

In contrast to the 500-nm wavelength of the lidar, the sensitivity of the 8-mm cloud-radar wavelength to detect particles increases in the size range from 1 μm to approximately 10 mm. Signals from particles smaller than 1 mm are rather low. For this reason the measurement sensitivity for particles smaller than 1 mm was scaled by a factor of 1000 (see grey line in Figure 1). For droplets with radii lager than 1 mm sensitivity raises quickly, as shown by the black curve in Figure 1. This curve also shows that mm-sized precipitation droplets do affect the radar signal as strong as μm-range particles affect the lidar signal. For the detection of clouds the wavelength of 8 mm at which the cloud radar operates is well suited.

The difference in the measurement sensitivity of radar and lidar is illustrated in Figure 2 that shows a measurement performed at TROPOS on 9 September 2011, 1200 to 1600 UTC. Figure 2 (a) displays the lidar measurement that was performed at a wavelength of 532-nm wavelength. The lidar observation shows that a well-mixed planetary boundary layer was present between the ground and 1.5-km height throughout the measurement. Within the boundary layer, convective clouds, indicated by dark red colours, occur below 1-km height. At heights between 1.5 and 3 km a slowly descending stratus layer was observed. During most of the measurement time, the lidar beam was attenuated by the liquid water droplets in the stratus cloud. Only during gaps in the cloud cover higher clouds were detected. The lidar signal does not provide information about the cloud interior or about cloud or

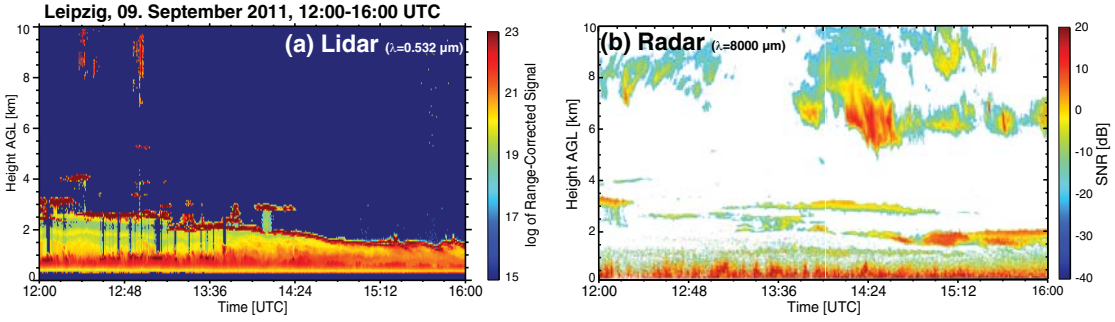

Figure 2: a) TROPOS lidar measurement at 532 nm wavelength and b) TROPOS cloud radar measurement at 8 mm wavelength of 9 September 2011, 1200–1600 UTC.

aerosol layers present above the cloud. The hydrometeors extinct the transmitted laser pulses, so that the vertical structure of clouds cannot be determined.

Figure 2 (b) shows the measurement of a cloud radar for the same time period. In contrast to the lidar the radar measurement captures the vertical structure of the clouds. At heights above 4 km, where scarce information was obtained with the lidar, a widespread cirrus cloud occurred. Also we see that the descending stratus cloud layer, whose base was observed also with the lidar, consisted of several layers. The radar observation also shows that these cloud layers feature low vertical extents. The radar measurement also suggests that the aerosol layers at below 1.5-km height were observed as well. As seen in Figure 1, aerosol particles are too small do be detected with radar. Instead, the radar detects so-called atmospheric plankton, i.e., insects or leaf litter that follow the atmospheric motions [*Russell and Wilson*, 1996].

2.2 Radar theory for a single-target scattering process

The MIRA-35 cloud radar operated at TROPOS (see Section 3.1) emits pulses of electromagnetic radiation of a wavelength $\lambda = 8\,\mathrm{mm}$ with a transmitting power P_t. Cloud hydrometeors and other targets in the atmosphere scatter the radiation.

The radar measurement principle is demonstrated in Figure 3. From the time shift Δt between transmittance of the pulse and the detection of the backscattered power P_r the range z at which the scattering event occurred can be calculated, given a constant propagation speed c of the pulse:

$$z = \frac{c}{2\,\Delta t} \tag{2.1}$$

In the case of electromagnetic radiation as used by a radar, c is the speed of light.

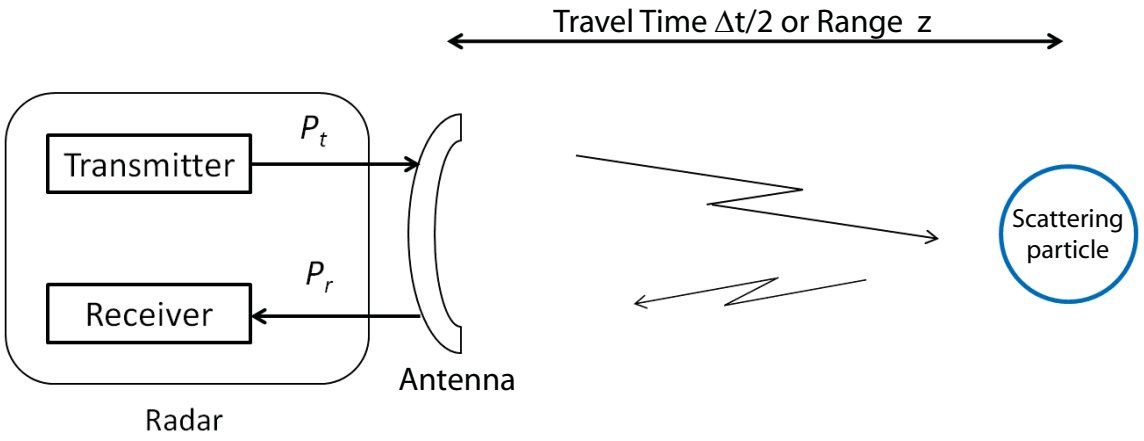

Figure 3: Draft of the radar-measurement principle.

Range z can also transformed into height h by

$$h = z \sin(\delta) \tag{2.2}$$

when the elevation angle δ is known.

The power P_r retrieved from a single target can be calculated with Equation 2.3 [*Peters and Görsdorf*, 2010]:

$$P_\mathrm{r} = C_1 \frac{1}{z^4} \tau(z)^2 \sigma \tag{2.3}$$

The constant C_1 describes the system characteristics that depend on the transmitted power P_t, the used wavelength λ, and the beam divergence ϕ:

$$C_1 = \frac{P_\mathrm{t} \pi \lambda^2}{4 \phi^2} \tag{2.4}$$

Further parameters which influence P_r are the range z between radar and scattering particle, the transmittance $\tau(r)$, and the backscattering cross-section σ of the target. $\tau(z)$ characterizes the extinction of the electromagnetic waves in the atmosphere. The scattering properties of the target are described by the backscattering cross-section σ [*Peters and Görsdorf*, 2010]:

$$\sigma = \frac{\pi^4}{\lambda^4} |K|^2 D^6 \tag{2.5}$$

The backscattering cross-section σ is determined by the refractive properties of the target which are described by $K = |\frac{m^2-1}{m^2-1}|$ [*Montopoli and Mazano*, 2010] where m is the complex refractive index. The size of the particle is given by the diameter D.

2.3 Radar theory for volume-scattering processes

In practice, when radars are applied in meteorology, more than one scatterer contribute to the power P_r returned from a scattering volume. The received power then depends on the sum of all single scattered signals in the volume. So the signal is a function of the number, the sixth power of the diameter, and the shape of each scattering particle in a detected volume.

The definition of the scattering volume V of a radar is illustrated in Figure 4 and defined in Equation 2.6. ϕ specifies the divergence of the radar beam. The range resolution Δz specifies the depth of the volume V and z is the distance between instrument and volume:

$$V = \pi \left[\frac{D_0}{2} + z \tan \frac{\phi}{2} \right]^2 \Delta z \tag{2.6}$$

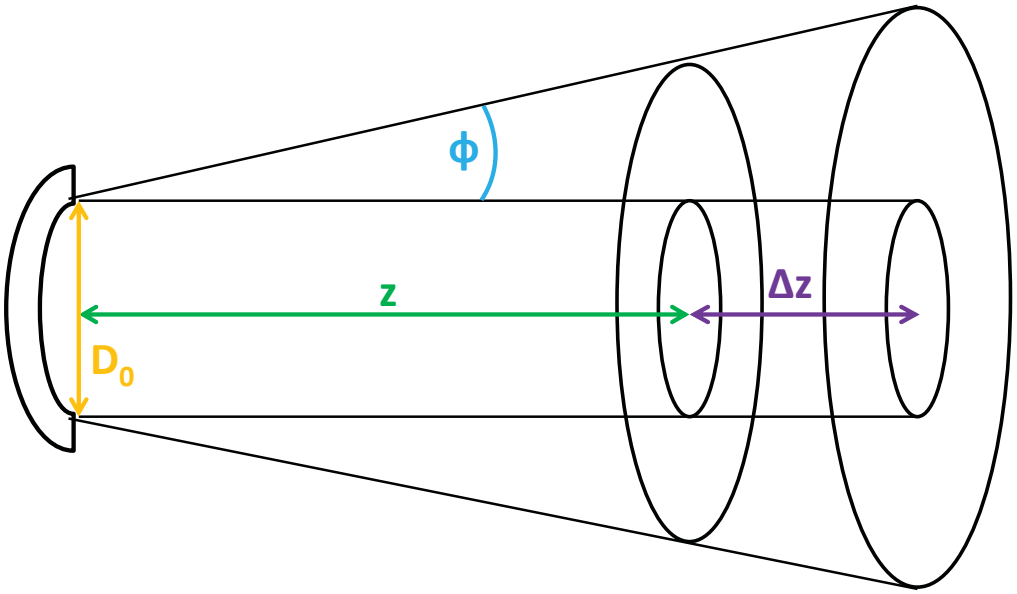

Figure 4: Illustration of a radar scattering volume: D_0 is the antenna diameter, ϕ is the beam divergence, z is the distance between radar and scattering volume, and Δz is the range resolution.

Figure 5 presents a comparison of the scattering volumes of radar and lidar as a function of height. The initial diameter D_0 of the radar pulse for this calculation is 1.2 m which is the antenna diameter. The beam divergence $\phi = 0.5°$ (8.7 mrad) and the range resolution $\Delta z = 15$ m. For the lidar pulse the initial diameter D_0 is 0.2 m, the beam width $\phi = 0.006°$ (0.1 mrad) and the range resolution $\Delta z = 30$ m. As a result of the beam divergence ϕ the scattering volumes increase with increasing distance to the instruments. The increase of the radar volume is much larger than the increase of the lidar volume. In Figure 5 can be seen that the radar detects about 100,000 m^3 at a range of 4 km, whereas the lidar only detects 30 m^3. At a range of 10 km the detected radar volume is about 700,000 m^3, whereas the one of a lidar is about 70 m^3. This fact needs to be considered when collocated lidar and radar measurements are compared.

When the volume contains i targets with a corresponding backscatter cross-section σ_i, the effective backscatter cross-section σ_v is defined as the sum of all σ_i in that volume:

$$\sigma_\mathrm{v} = \sum_V \sigma_\mathrm{i} \tag{2.7}$$

The detected radar signal P_r is thus a function of the sum of all single backscattered signals in the measured volume and is thus also proportional to the number of particles. Assuming that the whole scattering volume is homogeneously filled with targets, the single-target backscatter cross-section σ in Equation 2.3 can be replaced

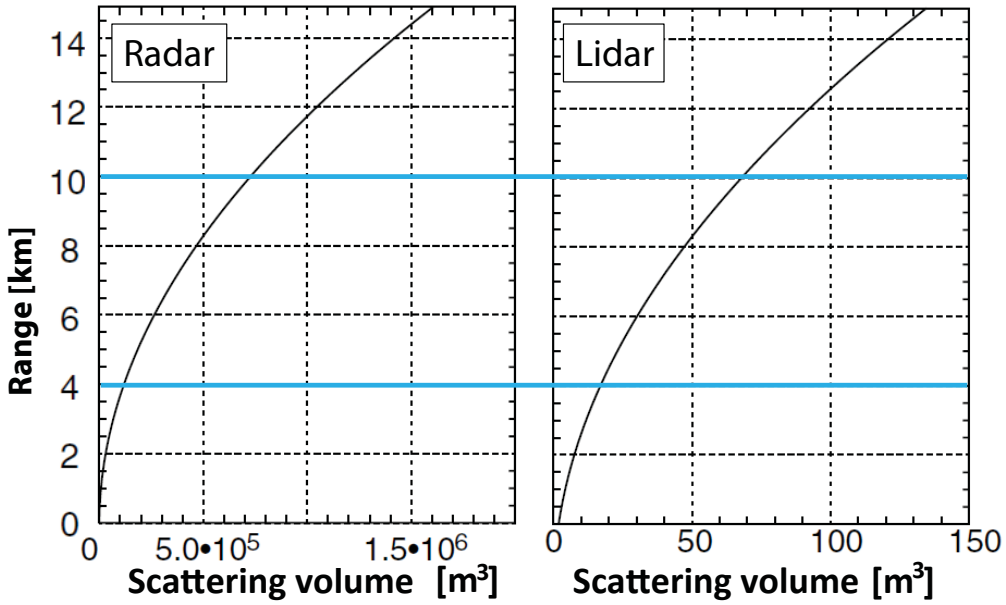

Figure 5: Scattering volume of a radar (left) and of a lidar (right) both as a function of height. The initial diameter D_0 of the radar pulse is 1.2 m, a beam divergence $\phi = 0.5°$ (8.7 mrad), and the range resolution is 15 m. The initial diameter of the lidar pulse is 0.2 m, the beam divergence $\phi = 0.006°$ (0.1 mrad), and the range resolution is 30 m.

by the specific scattering cross section η [*Peters and Görsdorf*, 2010]:

$$\eta = \frac{\sigma_\mathrm{V}}{V} \tag{2.8}$$

The specific backscatter cross section η is proportional to the effective scattering cross section σ_V of all particles in the volume. From the introduction of the specific backscatter cross-section η (Equation 2.8) and of the scattering volume that increases with the square of the range z (see Equation 2.6) a new version of the radar equation is obtained when the initial antenna diameter D_0 is neglected and it is assumed that $\tan\phi \approx \phi$ for small angles [*Peters and Görsdorf*, 2010]:

$$P_\mathrm{r} = C_2 \frac{1}{z^2} \tau(z)^2 \eta(z) \tag{2.9}$$

In equation 2.9, C_2 is again the range-independent radar constant:

$$C_2 = \frac{C_1 \Delta z \pi \phi^2}{4} = \frac{P_\mathrm{t}\, \pi\, \lambda^2\, \Delta z}{16\, \phi^2} \tag{2.10}$$

Equation 2.10 shows that P_r for volume-scattering processes does only depend on the inverse of the square of the range when atmospheric attenuation $\tau(z)$ is neglected and $\eta(z)$ is assumed constant. A wavelength-independent radar constant is obtained when the relation between beam divergence ϕ, wavelength λ, and effective antenna

Table 1: Reflectivity Z in linear scale and in dBZ (Equation 2.16) as a function of the droplet diameter when 10 droplets of the same diameter are present in the scattering volume of $1\,\mathrm{m}^{-3}$.

Droplet diameter	Reflectivity Z [$\mathrm{mm}^6\mathrm{m}^{-3}$]	Reflectivity Z [dBZ]
1 mm	10	10
100 μm	10^{-5}	-50
10 μm	10^{-11}	-110
1 μm	10^{-17}	-170

aperture A_e is considered, which is [*Peters and Görsdorf*, 2010]

$$\frac{1}{\phi^2} = \frac{4\,A_\mathrm{e}}{\lambda^2}. \tag{2.11}$$

Inserting Equation 2.11 into Equation 2.10 yields the wavelength-independent version of the radar constant

$$C_3 = \frac{P_\mathrm{t}\,\pi\,A_\mathrm{e}\,\Delta z}{4}. \tag{2.12}$$

The backscatter cross-section σ for cloud droplets is small in relation to the used wavelength λ. So Rayleigh-theory can be applied to describe the backscatter cross-section [*Gunn and East*, 1954]. Because the backscattered signal is the sum of all backscatter signals of all particles in the sampling volume the scattering cross-section η can be calculated similar as for single targets (see Equation 2.5) [*Görsdorf*, 2009]:

$$\eta = \frac{\pi^5}{\lambda^4}\,|K|^2\,Z \tag{2.13}$$

In Equation 2.13 Z is the reflectivity factor of the detected hydrometeors, and $|K|$ describes the mean refraction characteristics of all targets in the sample volume.

Z is a function of the particle size and the number of the detected hydrometeors:

$$Z = \sum_{i=0}^{\infty} D_\mathrm{i}^6 = \int_0^\infty N(D)\,D^6\,dD \tag{2.14}$$

Assuming that the targets in the sample volume are spherical liquid water droplets the refraction characteristics K^2 can be described with $K^2_{\mathrm{H_2O}} = 0.9$ [*Montopoli and Mazano*, 2010], so that their reflectivity factor can be calculated:

$$Z = \frac{\lambda^4}{\pi^5 K^2_{\mathrm{H_2O}}}\eta \tag{2.15}$$

Table 1 displays the reflectivity for liquid water droplets with a number concentration of 10 m^{-3} for four different droplet diameters. The range of the calculated

reflectivity spans over 18 orders of magnitude as is shown in the second column of Table 1. To improve the handling of the large range of orders of magnitudes the reflectivity is usually given in dBZ that is defined as [*Montopoli and Mazano*, 2010]

$$\mathrm{dBZ} = 10 \log_{10} \frac{Z}{Z_0}. \tag{2.16}$$

Equation 2.16 is a scaling function. The measured reflectivity is normalized with respect to a reference reflectivity of $Z_0 = 1\,\mathrm{mm}^6\,\mathrm{m}^{-3}$. The reference reflectivity Z_0 corresponds to the reflectivity caused by a single droplet with diameter of 1 mm in a volume of $1\,\mathrm{m}^3$. The values of the reflectivity given in dBZ now only run over three orders of magnitude as the third column in Table 1 shows.

Due to the D^6-dependency the reflectivity does not give a direct relation to the droplet diameter. This fact is illustrated in Figure 6 that shows the droplet number concentration N as a function of droplet diameter D for three reflectivity values of $-55\,\mathrm{dBZ}$ (red curve), $-20\,\mathrm{dBZ}$ (black curve), and $0\,\mathrm{dBZ}$ (blue curve). As can be seen, a clear relationship between droplet size, droplet number, and reflectivity can hardly be found, especially for small droplets with diameters of below 0.01 mm. It is possible to derive one value of reflectivity for various monodisperse droplet size distributions. The reflectivity Z of $-55\,\mathrm{dBZ}$ for example is obtained for a droplet number concentration of $N = 3,000,000\,\mathrm{m}^{-3}$ and a droplet diameter of 10 μm, but

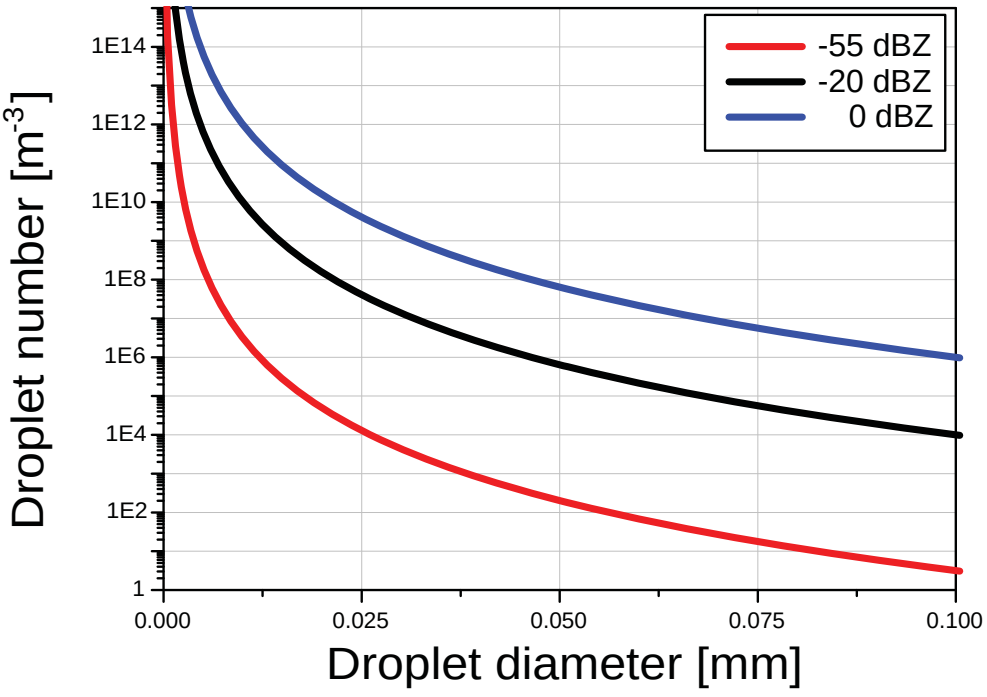

Figure 6: Relation between droplet diameter and droplet number for three values of reflectivity $Z = -55$ dBZ (red curve), $Z = -20$ dBZ (black curve), and $Z = 0$ dBZ (blue curve).

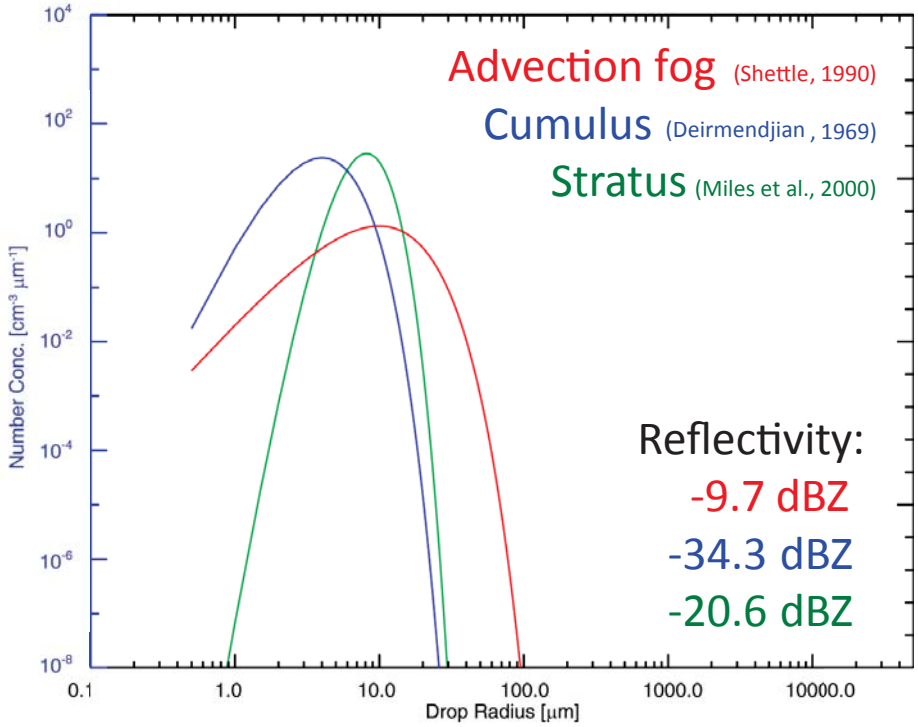

Figure 7: Calculated droplet size distributions of advection fog (red curve) [*Shettle*, 1990], a cumulus cloud (blue curve) [*Deirmendjian*, 1969], and a stratus cloud (green curve) [*Miles et al.*, 2000]. The reflectivities of the shown distributions were derived after Equation 2.14.

it is also obtained for a droplet number concentration of $3\,\mathrm{m}^{-3}$ at a diameter of $100\,\mu\mathrm{m}$.

In reality, droplet size distributions are not monodisperse. They are usually described by gamma or logarithmic distribution functions [*Deirmendjian*, 1975, *Shettle*, 1990, *Miles et al.*, 2000] which is further described in Section 4.2. Examples of droplet number distributions for three different cloud types are given in Figure 7. Besides the distribution curves, Figure 7 contains also the calculated reflectivities of the three cloud types that were calculated after Equation 2.14.

The largest reflectivity is obtained for advection fog (red curve), even though droplet concentration is much lower as for cumulus and stratus. Due to the D^6-dependence of the reflectivity a value of $Z = -9.7\,\mathrm{dBZ}$ is obtained. The stratus cloud droplet size distribution (green curve) yields a reflectivity of $Z = -20.6\,\mathrm{dBZ}$. Even though, the cumulus (blue curve) has a droplet size distribution that is similar to the one of the stratus, it only yields a reflectivity of $Z = -34.3\,\mathrm{dBZ}$. The size distribution of the stratus is slightly shifted to larger diameters. A cumulus is a convective cloud. During convective processes a large number of new droplets is formed in updraft regions. Small droplets produce small reflectivity values, so the reflectivity of the cumulus is more than one order of magnitude lower than the one of the stratus.

The three example clouds presented in Figure 7 represent approximately the range of reflectivities produced by ambient clouds that do not contain drizzle droplets. Newly formed clouds with high numbers of small droplets will extend the reflectivity range to lower values. Larger reflectivities would occur for aged clouds that already formed drizzle via droplet coagulation.

2.4 The Doppler velocity

Often radars feature the ability to measure the frequency shift between transmitted radar pulse and backscattered signal. This frequency shift, denoted Doppler frequency, is caused by moving targets. Using the measurement of the Doppler frequency shift f_d, the Doppler velocity v_d can be calculated if the wavelength of the emitted radiation is known [*Rinehart*, 1997]:

$$v_\mathrm{d} = \frac{f_\mathrm{d}\,\lambda}{2} \tag{2.17}$$

In Equation 2.17 v_d denotes the radial velocity of the target, i.e., the motion of the target along the line of sight of the radar antenna. In the case of a vertically pointing radar the Doppler velocity v_d provides information about the fall speed of the targets, e.g., hydrometeors. In theory v_d is used to determine the size of the falling hydrometeors assuming that the fall speed of a droplet is proportional to its mass and so to its diameter.

2.5 The Doppler spectrum

Usually numerous targets are present in the sample volume of the radar. Each of the individual targets then produces a frequency shift according to its radial velocity. Measuring the returned power in any interval of the frequency shift allows for the detection of the Doppler spectrum. This is illustrated in Figure 8 that shows a sketch of the Doppler spectrum. The frequency axis is already converted to a velocity axis with Equation 2.17.

From the Doppler spectrum the reflectivity Z can be calculated [*Görsdorf*, 2009]:

$$Z = \int_{v_\mathrm{min}}^{v_\mathrm{max}} S(v_\mathrm{d})\,\mathrm{d}v_\mathrm{d} \tag{2.18}$$

The integral of the spectral power S_{v_d} is called the 0-moment of the Doppler spectrum which equals the reflectivity Z. Further the first moment, Equation 2.19, and the second moment, Equation 2.20, of the Doppler spectrum can be calculated

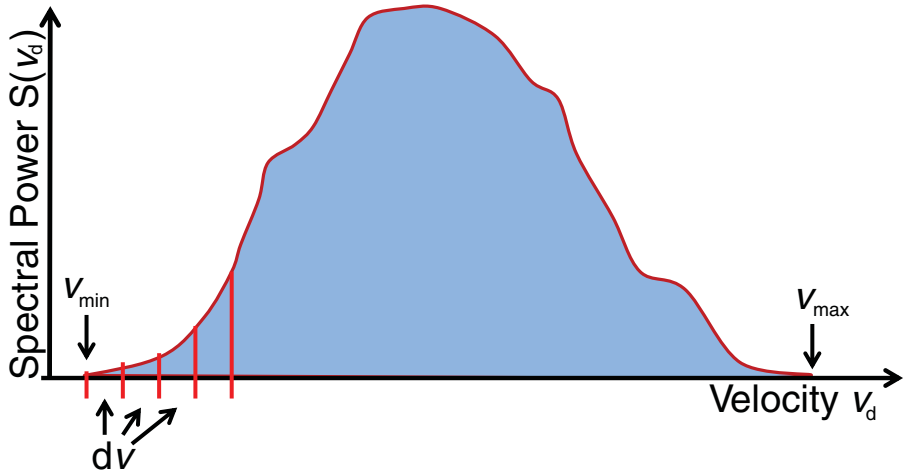

Figure 8: Sketch of a Doppler spectrum. Shown is the spectral power $S(v_\mathrm{d})$ as a function of the Doppler velocity v_d. v_min and v_max denote the minimum and the maximum velocities, at which $S(v_d) > 0$. $\mathrm{d}v$ is the velocity resolution.

[*Görsdorf*, 2009]:

$$V = \frac{1}{Z} \int_{v_\mathrm{min}}^{v_\mathrm{max}} v_\mathrm{d}\, S(v_\mathrm{d})\, \mathrm{d}v_\mathrm{d} \tag{2.19}$$

$$W^2 = \frac{1}{Z} \int_{v_\mathrm{min}}^{v_\mathrm{max}} (v_\mathrm{d} - V)^2\, S(v_\mathrm{d})\, \mathrm{d}v_\mathrm{d} \tag{2.20}$$

The first moment of the Doppler spectrum is the mean Doppler velocity V. It corresponds to the mean radial velocity in the sample volume.

The second moment is called the Doppler width W^2. It corresponds to the variance of the Doppler spectrum. The Doppler width basically is a measure of the width of the spectrum of detected velocities. It also can be a measure of the number of modes the targets size distribution has. A mono-modal distribution gives a small spectral width. A distribution that has several modes yields a lager spectral width, as illustrated in Figure 9. The spectral width is also influenced by turbulent motion of the targets in the sample volume. With increasing turbulence the spectral width increases.

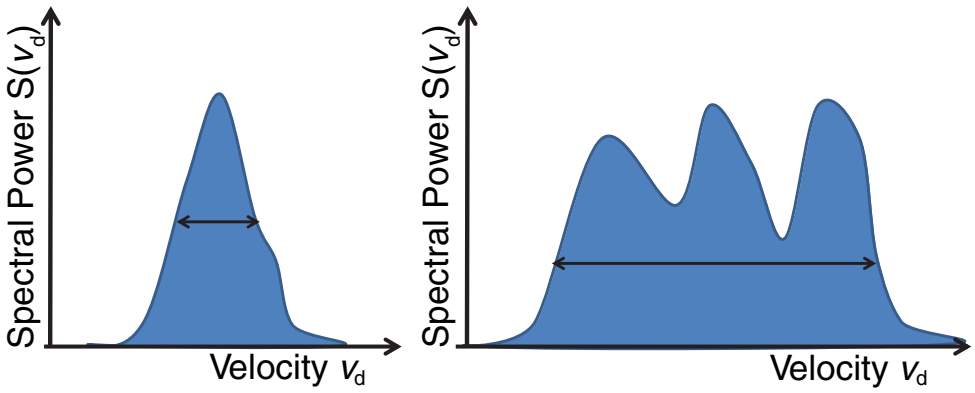

Figure 9: Draft of the Doppler width. It shows the relation between the Doppler width W^2, described by the arrows, and the number of modes of the droplet size distribution.

3 Instruments

In this Chapter the instruments are introduced that provided the data used in the underlying study. The instruments are all operated at TROPOS in the mobile research facility Leipzig Aerosol and Cloud Observations System (LACROS). LACROS comprises a unique set of active and passive remote-sensing instruments. Most of the instruments are containerized and available for application in field campaigns. The whole instrument suite of LACROS is shown in Figure 10 and only briefly described below.

The essential instrumentation for cloud observations are the 35-GHz cloud radar MIRA-35 and the microwave radiometer HATPRO. They are installed into a sea container that is shown in Figure 11. LACROS also comprises the multiwavelength-Raman-polarization lidar MARTHA (Multiwavelength Tropospheric Raman lidar for Temperature, Humidity, and Aerosol profiling) [*Mattis et al.*, 2002], the portable high-spectral-resolution lidar BERTHA (Backscatter Extinction Ratio Temperature, Humidity Lidar), Polly^{XT} (POrtabLe Lidar sYstem) [*Althausen et al.*, 2009], a ceilometer CHM 15kx, and the Doppler lidar WiLi (Wind Lidar) [*Engelmann et al.*, 2008]. Passive instrumentation which helps to interpret the active remote measurements consists of an Aerosol Robotic Network (AERONET) Sun photometer [*Holben et al.*, 1998], the microwave radiometer HATPRO [*Rose et al.*, 2005] that includes

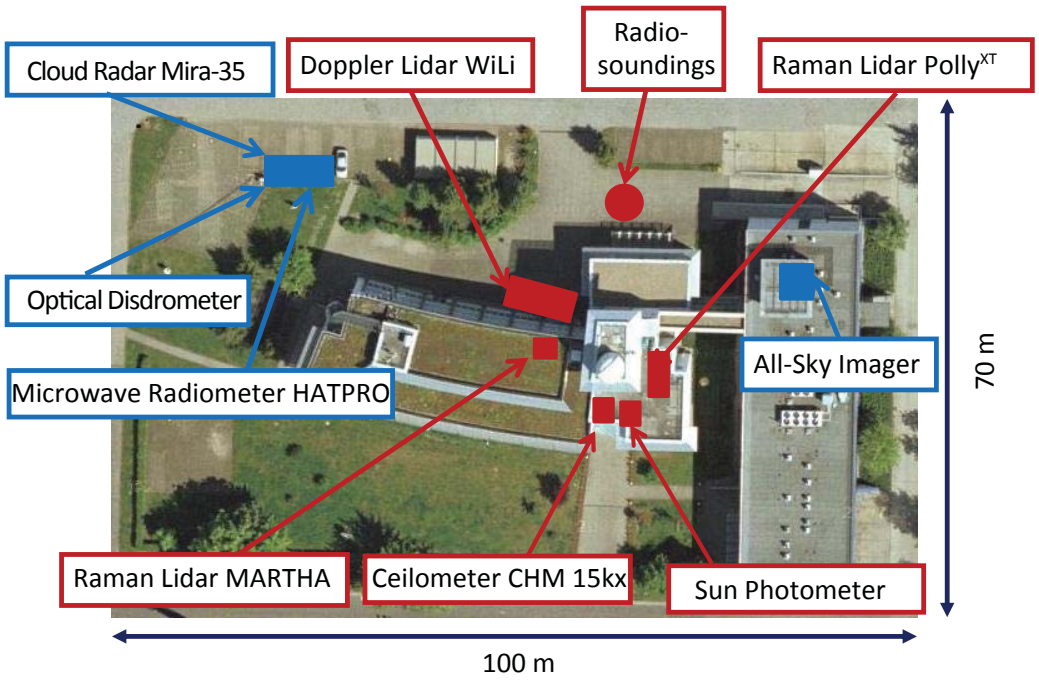

Figure 10: LACROS, Leipzig Aerosol and Cloud Research Observations System, is the network of the aerosol and cloud remote sensing systems at TROPOS.

also two infrared radiometers, and an all-sky imager. Meteorological surface data and radiosondes are available in addition. It is planned to become part of BSRN (Baseline Surface Radiation Network) [*Ohmura et al.*, 1998] that aims at obtaining quality-assured surface radiation measurements. For the determination of precipitation properties an optical disdrometer [*Jaffrain et al.*, 2011] records the velocity and size distribution of falling hydrometeors in the size range from 0.1 mm to 10 mm at 4 m above ground.

The instruments actually used for this study are explained more detailed in the following Sections 3.1 to 3.4.

3.1 Cloud radar MIRA-35

The cloud radar operated at TROPOS is the 35-GHz MIRA-35 of the Metek company. The instrument is located outside the TROPOS main building and is installed into a sea container as Figure 11 shows. The diameter of the radar antenna is 1.2 m, the transmitting power is 30 kW. The antenna has a clutter fence to protect the antenna from ground clutter echoes. Data is recorded with a temporal resolution of 10 s within a height range from 150 m to 15000 m above ground and with a spatial resolution of 30 m. The instrument measures the backscattered power, the radial velocity along the line of sight of the antenna by means of the Doppler spectrum, and the depolarization ratio of the backscattered power returned from clouds and precipitation. The velocity-resolution of the Doppler spectrum is 8 $\mathrm{cm\,s^{-1}}$ and the first range at which a signal is detected is at 250 m. The depolarization ratio of

Figure 11: The cloud radar Mira-35 and the microwave radiometer HATPRO installed in a sea container at TROPOS.

backscattered power is not further discussed in this work.

According to Equation 2.12 the system constant C_3 of the cloud radar must be known in order to derive the equivalent reflectivity of liquid water droplets introduced in Equation 2.15. This absolute calibration was given by the manufacturer of the radar.

3.2 Doppler-lidar WiLi

The Doppler lidar WiLi (see Figure 12) measures the Doppler shift of light at the wavelength $\lambda_0 = 2022\,\mathrm{nm}$ to detect the motion of aerosol and cloud particles along the line of sight of the laser beam [*Engelmann*, 2009]. For aerosol particles and small cloud droplets the inertial forces caused by changes in the wind velocity can be neglected. In this case, the measured particle motions correspond to the actual atmospheric wind velocity. The transmitter and receiver of WiLi are usually pointed to the zenith in order to measure the aerosol particle vertical velocity.

The Doppler-velocity resolution of Wili is approximately 6 $\mathrm{cm\,s^{-1}}$. Due to the optical setup of the Doppler lidar, the measurement of the Doppler velocity is only possible at heights above approximately 450 m.

3.3 Microwave radiometer HATPRO

The microwave radiometer HATPRO of the Radiometer Physics GmbH (RPG) is a passive remote sensing instrument. The instrument is located outside the TROPOS main building and is installed into the same ocean container as the cloud radar as shown in Figure 11. It detects microwave radiation emitted by liquid water, oxygen, and water vapour [*Rose et al.*, 2005, *Crewell et al.*, 2010]. Water vapour

Figure 12: The Doppler lidar WiLi installed in a container.

and oxygen have strong rotational transitions in the size range from 20-50 GHz. The broadening of the absorption bands is influenced by the atmospheric temperature and the number density of the molecules. Measurements along the edges of these absorption bands provide information about temperature that influences the width of the absorption band, and atmospheric gases that influences the intensity of the absorption band (e.g., water vapour [*Crewell et al.*, 2010]).

These multi-channel measurements are performed in the range of the absorption lines of oxygen 22.2-31.4 GHz and water vapour 51.3-58.0 GHz. From these measurements temperature and humidity profiles as well as the liquid water path (LWP) W_p can be determined. The liquid water path is the total atmospheric integrated liquid water content.

The radiometer can measure the liquid water path directly. It is derived with a retrieval that correlates the measured brightness temperatures with calculated ones from a radiation transfer program. An equation for the calculation for the LWP from data of a two-channel microwave radiometer is shown in [*Crewell et al.*, 2010]:

$$W_\mathrm{p} = b_0 + b_1 T_{24} + b_2 T_{31} \tag{3.21}$$

With Equation 3.21 the LWP can be determined from the measured brightness temperatures at 24 GHz and 31 GHz and three calibration factors b_0, b_1, and b_2. The factors b_0, b_1, and b_3 are derived from radiative-transfer calculations that are based on atmospheric soundings. Various retrieval algorithms for different radiometer systems and atmospheric parameters do exist, a good overview is presented in [*Löhnert and Crewell*, 2003]. For the underlying study the retrievals provided by the manufacturer of the HATPRO are applied.

3.4 Ceilometer

The Jenoptik Ceilometer CHM15kx, shown in Figure 13, is a zenith-pointing commercial backscatter lidar system [*Wiegner and Geiß*, 2012]. It emits laser pulses at 1064 nm with a typical pulse energy of 8 μJ and a pulse repetition frequency of about 6500 Hz. The beam divergence is 0.33 mrad and the field of view is 1.8 mrad. The temporal resolution of the data is 30 s and the range resolution is 15 m. 1064 range gates are detected yielding a maximum range of 15.36 km.

The Ceilometer basically provides cloud base heights. The backscatter coefficient β and the extinction coefficient α of aerosols and clouds can be estimated from the Ceilometer measurements, too. The coefficients β and α determine the optical properties of the aerosol particles and cloud hydrometeors [*Weitkamp*, 2005].

Figure 13: The Jenoptik Ceilometer CHM15kx installed on the roof at TROPOS.

3.5 Measurement example of 27 December 2011

This section aims at the illustration of the theoretical background presented in Chapter 2 by means of a measurement example. The measurement is introduced in Figure 14. It presents a radar measurement of a drizzling stratus cloud that was observed at TROPOS on 27 December 2011 between 1400 and 1700 UTC.

In Figure 14 (a) the intensity of the detected signal-to-noise ratio (SNRg) in dB is shown. The signal-to-noise ratio corresponds to P_r in Equation 2.9. It is a product of all scatters, including clouds, precipitation, insects, and other plankton. Overall, the drizzling stratus clouds at altitudes below 1.5 km height dominates the measurement.

Figure 14 (b) shows the corresponding equivalent reflectivity of hydrometeors. The calculation is based on the assumption that the hydrometeors are spherical liquid water droplets, following Equation 2.9. Contributions of plankton were removed by the software of the radar manufacturer.

Throughout the measurement period the observed reflectivity is low and rather constant in the cloud top region. The reflectivity of the hydrometeors varies around −30 dBZ. According to Figure 7 such values are produced by stratus or cumulus clouds. This suggests that the actual cloud layer that produced the drizzle is present in this region. Already within 100 to 200 m distance from cloud top the temporal and spatial variability of the reflectivity increases. Values vary strongly between −50 dBZ and 0 dBZ. This is likely caused by drizzle droplets that precipitate out of the upper cloud layer. According to Figure 6 and Table 1, 0 dBZ already can be produced by a concentration of 1 droplet of 1 mm diameter in 1 m^{-3}. In turn, only a very low concentration of precipitating droplets is needed to produce a reflectivity of −50 dBZ, as it was observed between 1430 and 1530 UTC. It is thus likely that the drizzle droplets were evaporating during that time period.

More information about the size of the observed droplets may be obtained if their

fall velocity would be known. With MIRA-35 also the Doppler spectrum of the hydrometeors can be measured. In case of a zenith-pointing measurement, the Doppler velocity corresponds to the terminal fall velocity of the detected target population. The terminal fall velocity is the equilibrium fall velocity at which gravitational force and drag force of a particle balance out. All radar measurements used within the underlying study were zenith-pointing.

The mean Doppler velocity for the example measurement introduced in Figure 14 is shown in Figure 15. The Doppler velocity measurement shows positive velocities in the cloud top region, i.e., atmospheric updrafts occurred in this part of the cloud and dominated the terminal fall velocity of the observed droplets. This corroborates the hypothesis that mostly small cloud droplets were present. 100 to 200 m below

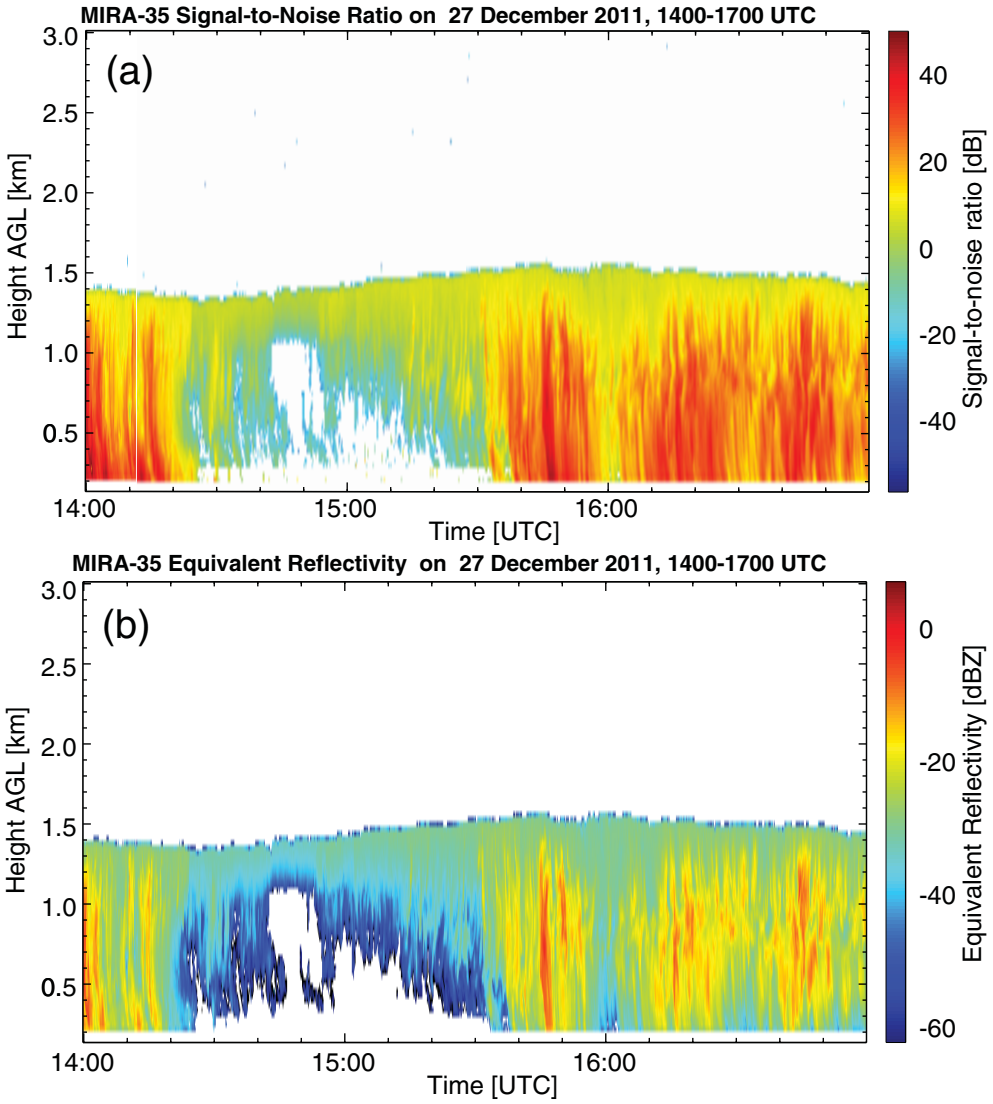

Figure 14: Measurement of the cloud radar Mira-35 at TROPOS of 27 December 2011 from 1400 till 1700 UTC. Figure (a) shows the signal to noise ratio SNR, (b) the calculated reflectivity for water droplets Ze. The colour tables point out the intensity in dBZ.

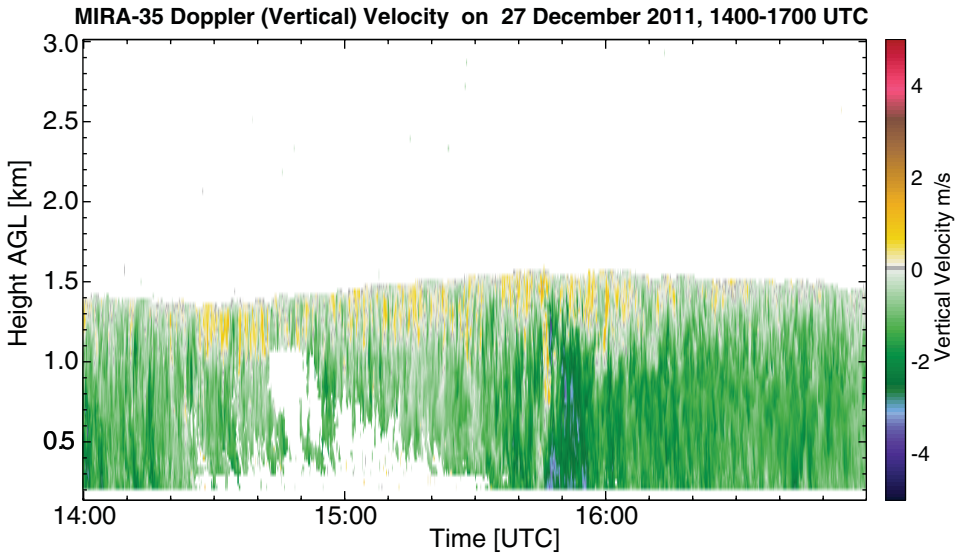

Figure 15: Vertical velocity measured with Mira-35 on 27 December 2011 at TROPOS. The observation spans over the same time range as the ones presented in Figure 14. Negative values correspond to downward motion.

cloud top, velocities are predominantly negative, indicating downward motion of the observed droplets. Only around 1540 UTC an updraft occurred. At around 1550 UTC, when strongest reflectivities were observed (see Figure 14 (b)), the fall velocities are highest with values around $-3\,\mathrm{m\,s^{-1}}$. Droplets were thus largest in this region. In the drizzle region between 1430 UTC and 1530 UTC where low reflectivities were observed, also the fall velocity is rather low. This corroborates that only slowly falling small droplets were present during this time period.

The radar detects the Doppler spectrum at each range gate of a measurement. In Figure 16 (a) a vertical profile of the Doppler spectrum measured at 15:37:38 UTC (during the measurement introduced in Figure 14) is shown.

The vertical profile of the Doppler spectrum highlights the variability of the target terminal velocities with altitude. In the highest 200 m of the vertical profile it can be seen that the velocity accumulates around $0\,\mathrm{m\,s^{-1}}$ and that the signal intensity is low. As mentioned above, it is likely that only small cloud droplets are present in this height range. It can be seen in Figure 14 (b) that low reflectivity values are shown at the top of the stratus. In comparison to the droplet size distributions in Figure 6 the reflectivity at cloud top relates to those produced by stratus or cumulus clouds. Higher reflectivities are shown in the region where drizzle is assumed. Also the observed vertical velocities are indicating that the droplets are small enough to be moved upward by atmospheric motions.

A more-detailed view on the Doppler spectra is shown in the four subfigures below the vertical profile of the Doppler spectrum in Figure 16. The spectrum at 1528.98 m height (Figure 16 (b)) is narrow with a high contribution of positive velocities. This again corroborates the impression that the cloud droplets in this height range were

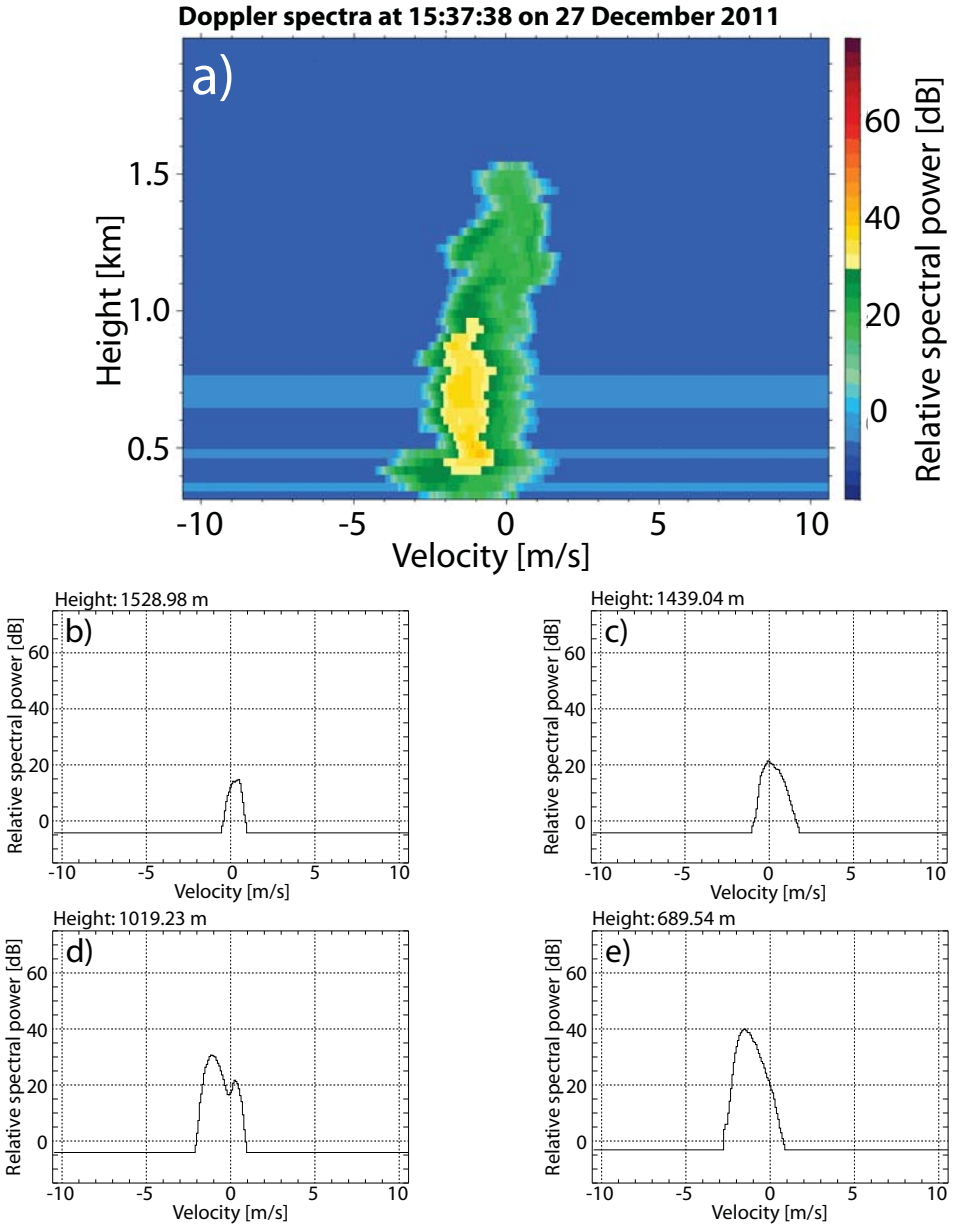

Figure 16: Doppler spectra measured during the same time periods as shown in Figures 14 and 15 on 27 December 2011, 15:37:38 UTC. (a) Vertical profile of the Doppler spectrum. (b) – (e) Doppler spectra measured at 1528 m, 1439.04 m, 1019.32 m, and 689.54 m height, respectively.

small and followed atmospheric motions.

The Doppler spectra at 1439.04 m height (Figure 16 (c)) is wider and shows increased signal intensities. Overall, the spectrum is shifted to slightly lower velocities. The increased signal intensities and the lower velocities suggest that droplet size increases.

Figure 16 (d) shows the Doppler spectrum at 1019 m height. The spectrum shows a bimodal shape. Thus, the drizzle mode can now be separated from the cloud mode. This impression is corroborated by the increased fall speed, the negative

velocity values, and the signal intensity of the left mode. The cloud mode still shows intensities and positive velocities similar to Figure 16 (b) .

At lower heights of 689 m (see Figure 16 (e)) in the vertical profile of the spectrum it can be seen that the spectral width of the drizzle mode increases. Also its intensity increases and the velocity is shifted further forwards negative values. This effect is most likely caused by the increased size of the drizzle droplets.

The measurement example demonstrates that the Doppler spectra contain information about the droplet number concentration and the droplet size. However, in order to derive a quantitative estimate of droplet size and droplet size distribution a relation between the Doppler velocity and droplet size is required. A solution of this problem is described in the following Chapter 4.

4 Simulation of radar signals

In Section 2.2 and 2.3 it was shown that the equivalent radar reflectivity is a function of the particle size and number. For a given droplet size distribution, the corresponding reflectivity can directly be calculated. However, a radar measures the reflectivity as a function of Doppler velocity. To relate the spectral power of the Doppler spectrum to the spectral power of the size distribution it is necessary to find a relation between the fall velocity and the size of the hydrometeors. Under the assumption, that the observed Doppler velocity equals the fall speed of the cloud hydrometeors, the Doppler spectrum can then be directly converted into the size distribution.

From the size distribution further cloud microphysical properties are determined from the droplet size distribution, e.g., the cloud liquid water content

$$q_{\mathrm{l}} = \rho_{\mathrm{H_2O}} \int_0^\infty \frac{4}{3}\pi N(r) r^3 \,\mathrm{d}r \tag{4.22}$$

or the effective droplet radius

$$r_{\mathrm{e}} = \frac{\int_0^\infty N(r) r^3 \mathrm{d}r}{\int_0^\infty N(r)\pi r^2 \,\mathrm{d}r}. \tag{4.23}$$

The effective radius, which is the ratio of the total volume to the total area of a particle size distribution, is an important parameter in radiative transfer calculations [*Hansen and Travis*, 1974].

An approach to relate the Doppler spectrum to the droplet size distribution is presented in Section 4.2. In Section 4.3.1 and 4.3.2 the approach is applied to selected cases by means of simulations.

4.1 Relation between droplet size distribution and Doppler spectra

The reflectivity Z can be calculated from a given droplet size distribution by applying Equation 2.14. It can as well be calculated from the Doppler spectrum (Equation 2.18) assuming that the Doppler velocity v_{d} equals the droplet fall velocity v_{f} which is in this Chapter donated v:

$$\int_0^\infty N(D)\, D^6 \, dD = Z = \int_{v_{\min}}^0 S(v) \,\mathrm{d}v \tag{4.24}$$

For a zenith-pointing radar and the assumption of absence of air motion, the Doppler-spectral power $S(v)$ can be expressed as a function of D:

$$S(v) = S(D(v)) = N(D(v))\, D(v)^6 \frac{\partial D(v)}{\partial v} \tag{4.25}$$

Vice versa, the size-related spectral power $S(D)$ can be transformed into the Doppler-spectral power [*Atlas et al.*, 1973]:

$$S(v(D)) = N(v(D))\, D(v(D))^6 \frac{\partial D(v(D))}{\partial v(D)} \tag{4.26}$$

The Doppler spectrum now can be calculated for a given droplet size distribution. The final equation for the reflectivity Z is derived by inserting Equation 4.25 into Equation 2.18:

$$Z = \int_0^\infty N(D(v))\, D(v)^6 \frac{\partial D(v)}{\partial v} dv \tag{4.27}$$

In order to implement the substitution of v by $D(v)$ and vice versa a relation between droplet diameter and the corresponding fall velocity must be known. Various parametrisations exist and two of the parametrisations are shown in Figure 17 graphically. The one provided from *Beard* [1985] is a complex parametrization that can be pressure corrected and is valid for a large droplet radius size range. The second parametrization is simpler linear one and just valid from 45 μm to 400 μm. This parametrization is used in the by *Frisch et al.* [1995] provided method for the determination of microphysical properties of drizzle droplets. For this simulation studies the parametrization from *Beard* [1985] is used because it is valid for a large size range. The parametrization provided by *Beard* [1985] gives a power-law relationship between v and D:

$$v = v_0 \left(\frac{\rho_0}{\rho}\right)^{0.373+0.025D} \tag{4.28}$$

In Equation 4.28 ρ_0 is the reference density of $1.194\,\mathrm{kg\,m^{-3}}$, ρ is the density of the air surrounding the droplet, and v_0 is an empirically-derived reference fall velocity that is defined as

$$v_0 = 5.984 + 0.8515\ln(D) + 0.1554\ln^2(D) + 0.03274\ln^3(D). \tag{4.29}$$

The parametrization is valid for small droplet radii starting from about 1 μm. Because the density of the air surrounding the droplet is accounted for, the parametrization is a function of height when it is applied to atmospheric conditions.

In Figure 17 the relationship between fall velocity and droplet diameter is illustrated. The fall velocity for droplets with radius $r = 10$ μm is small with

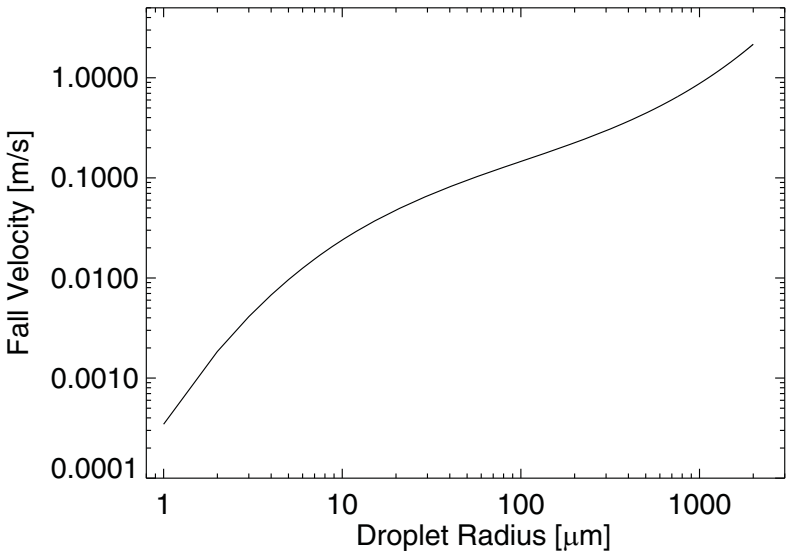

Figure 17: Relationship between droplet radius and fall velocity calculated for a density $\rho = 1000\,hPa$ (see Equation 4.29)

$v = 0.02\ \mathrm{m\,s^{-1}}$. Higher fall velocities of about $1\,\mathrm{m\,s^{-1}}$ are reached for a drop radius of around 1 mm.

The variables $D(v)$ and $\frac{\partial D(v)}{\partial v}$ in Equation 4.25 that are needed for the substitution of $S(v)$ can be derived from Equation 4.28.

4.2 Setup of the simulation

In this Section the setup of the simulation of Doppler spectra from given droplet size distributions is introduced. The results of the simulation give an impression on the shape of Doppler spectra produced by natural size distributions of cloud droplets and precipitation. For this purpose the spectral power distributions will be calculated for both $S(D)$ and $S(v) = S(D(v))$ to also get an impression on differences in the shapes of the two different spectra.

First, droplet number size distributions $N(D)$ must be obtained from which the spectral powers $S(D)$ and $S(v) = S(D(v))$ can be derived after Equations 2.14 and 4.25, respectively. Various parameterizations of droplet number size distributions are available in the literature. For this study, droplet size distribution for clouds were obtained from publications of *Deirmendjian* [1975] and *Miles et al.* [2000]. Both studies derived parameterizations of the size distributions from airborne in-situ measurements of clouds. The parameterizations were obtained by fitting the measurement to modified gamma functions.

The function used by *Deirmendjian* [1975] is

$$N(r) = A_{\mathrm{w}} r^{\alpha_w} \exp\left\{-B_{\mathrm{w}} r^{\Gamma_{\mathrm{w}}}\right\} \tag{4.30}$$

where r is the droplet radius, A_w, B_w and α_w are scaling factors, and Γ_w is the Gamma function.

The function used by *Miles et al.* [2000] is

$$N(D) = \frac{N_0}{\Gamma(\nu)} \left(\frac{D}{D_\mathrm{n}}\right)^{\nu^{-1}} \frac{1}{D_\mathrm{n}} \exp\left\{-\frac{D}{D_\mathrm{n}}\right\} \tag{4.31}$$

where D is the droplet diameter, N_0 is the total number concentration per unit volume, D_n is the nonphysical scaling diameter, ν is the shape parameter, and $\Gamma(\nu)$ is the Gamma function.

Drizzle droplet size distributions were not provided in the abovementioned publications. In order to enable the investigation of the effect of a drizzle mode on the Doppler spectra, a parameterization of *Van Zanten et al.* [2005] was implemented into the simulation. This parameterization is based on a fit of airborne in-situ measurements of drizzling stratus clouds to a logarithmic normal distribution:

$$N(D) = \frac{N_0}{D\sqrt{2\pi \ln^2(\sigma_\mathrm{g})}} \exp\left\{-\frac{(\ln D - \overline{\ln D})^2}{2\ln^2(\sigma_\mathrm{g})}\right\} \tag{4.32}$$

In Equation 4.32 D is also the droplet diameter, N_0 again the total number concentration per unit volume, and σ_g is the geometric standard deviation of the logarithmic normal distribution.

For the simulation the droplet size distributions $N(D)$ were calculated for $1\ \mu\mathrm{m} < D < 1000\ \mu\mathrm{m}$ in intervals of $\Delta D = 1\mu m$.

From $N(D)$ the spectral power $S(D)$ and thus the power spectrum as a function of $N(D)$ can be calculated directly after Equation 2.14. The calculation of the Doppler spectrum $S(v)$ requires the relationship between v and D, represented as $\frac{\partial D}{\partial v}$ in Equation 4.25. This relation was obtained numerically from Equation 4.28.

4.3 Simulation results

In this Section the results of the simulation of Doppler spectra from given droplet size distributions is provided. The first result, presented in Section 4.3.1, illustrates the simulated Doppler spectrum of a stratus cloud. A stratus cloud formation is frequently based on temperature inversion conditions [*Kraus*, 2000]. The shape of a stratus cloud droplet size distribution is narrow but in general the mean radius is lager than in cumulus clouds (see Figure 7).

In contrast to stratus clouds, cumulus clouds are formed during convective processes. This leads to the production of a large number of small droplets [*Kraus*, 2000] by activation of aerosol particles acting as cloud condensation nuclei. During the cumulus cloud formation process the droplets grow by coagulation and coalescence. For this reason the droplet size distribution is wider than the one of a stratus cloud.

Table 2: Parameters used for the parameterization of a stratus cloud after Equation 4.32. Data taken from *Miles et al.* [2000].

Reference in *Miles et al.*: *Hayasaka et al.* [1995]	N_0 [cm^{-3}]	ν	D_n [μm]
Stratus cloud droplet size distribution	148	17.3	1.0

Because of the large number of small droplets the mean radius of cumulus clouds is smaller than the mean radius of the stratus clouds. However, under the convective conditions present in cumulus clouds a fraction of the droplet population may grow to precipitation-sized droplets. To get an impression of the impact of precipitation on the Doppler spectrum the simulation of a drizzling cumulus cloud is presented in Section 4.3.2

4.3.1 Simulation of a stratus cloud

The cloud droplet size distribution of the stratus cloud was derived from the parametrization of *Miles et al.* [2000] that is given in Equation 4.31. Parameters that are used to calculate the droplet size distribution of the stratus that is used in this study are based on measurements of *Hayasaka et al.* [1995]. They are given in Table 2.

In Figure 18 the black curve illustrates the calculated droplet number concentration of the stratus cloud. The droplet size distribution is mono modal with a maximum at about 8 μm radius. The droplet radius ranges from 1 μm to 30 μm and the effective radius of the stratus droplets is 9.65 μm. With Equation 4.22 the liquid water content of the droplet size distribution can be calculated. The LWC of this

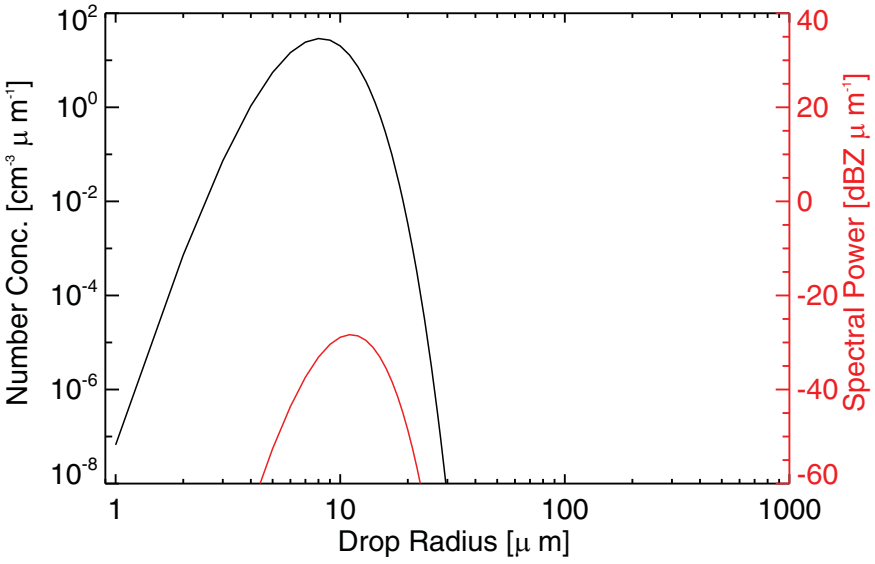

Figure 18: Simulated droplet size distribution (black curve) and power spectrum (red curve) of a stratus cloud as a function of the droplet radius.

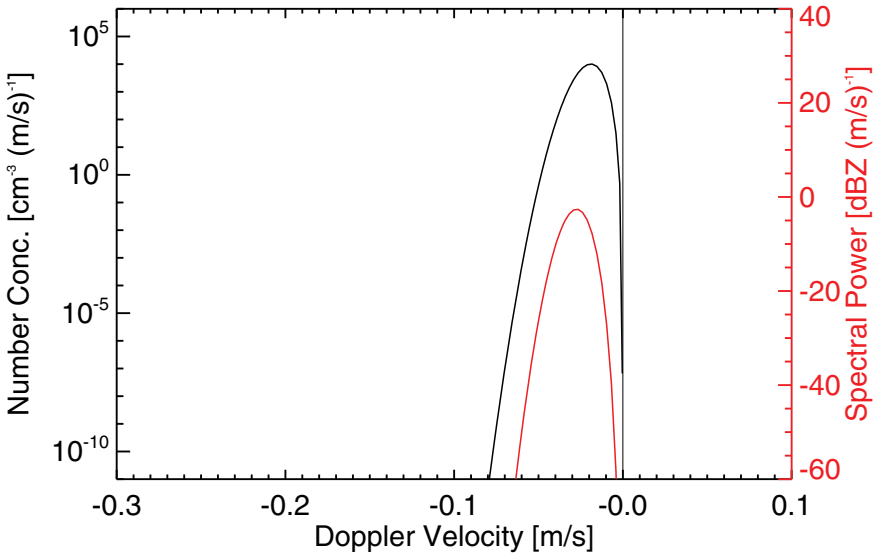

Figure 19: Simulated droplet size distribution (black curve) and Doppler spectrum (red curve) of a stratus cloud as a function of the Doppler velocity.

stratus cloud case is 0.474 g m^{-3}.

In Figure 18 the spectral power $S(R)$ derived from Equation 4.24 is illustrated by the red curve. The spectral shape is mono modal, too. However, the maximum of $S(R) = -25$ dBZ μm^{-1} is calculated for a droplet radius of about 11 μm. The overall shape of the power spectrum is more narrow than the one of the droplet size distribution. The peak of $S(R)$ is shifted to larger droplet radii compared to $N(R)$. These two facts show that a smaller number of droplets with large droplet radii have a larger influence on the spectral power than a large number of droplets with small droplet radii. This relates to the D^6-relationship of the radar signal that is described in Section 2.3 and already introduced in Equations 2.14 and 4.24. With the integral of the power spectrum over the whole radius size range of the droplet size distribution the reflectivity of the stratus is calculated as $Z = -20.595$ dBZ.

In Figure 19 the results of the Doppler spectrum calculated from the given droplet size distribution are illustrated. The droplet number concentration $N(v(D))$ as a function of velocity $v(D)$ in Figure 19 is illustrated by the black curve. The droplet-velocity distribution is again mono modal. The droplet size range of approximately 1 to 30 μm scales on a velocity range of 0 m s^{-1} to -0.08 m s^{-1}, whereby negative velocity values correspond to falling droplets.

The red curve in Figure 19 illustrates the Doppler spectrum of the stratus cloud. The Doppler spectrum is calculated with Equation 4.25. As can be seen in Figure 19 the shape of the Doppler spectrum is more narrow than the droplet-velocity distribution. The spectral power $S(v)$ of the Doppler spectrum is dominated by velocities in the range between 0 m s^{-1} and -0.065 m s^{-1}, i.e., by faster and thus larger droplets, with a maximum at about -0.04 m s^{-1}.

In Section 3.1 it was mentioned that the Doppler-velocity resolution of MIRA-35 is 8 cm s^{-1}. As can be seen from Figure 19, the whole spectrum produced by the stratus cloud droplet distribution spans over a velocity range of roughly 7 cm. Thus, a radar observation of a cloud featuring the presented droplet size distribution would, under absence of any turbulence, measure only a single peak in the Doppler spectrum.

4.3.2 Simulation of a drizzling cumulus cloud

The cloud droplet size distribution of the cumulus cloud was derived from the parametrization of *Deirmendjian* [1969] that is given in Equation 4.30. The parameters used for the simulation of the droplet size distribution are listed in Table 3. A precipitation mode was added to the droplet size distribution of the cumulus [*Van Zanten et al.*, 2005]. The precipitation mode is calculated with Equation 4.32 for the parameters listed in Table 3.

In Figure 20 the simulated droplet size distribution of the cumulus cloud and the added precipitation mode are illustrated (the black curve). The shape of the droplet size distribution is bimodal with the first maximum at a droplet radius of about 4 μm and a second maximum at a droplet radius of about 35 μm. The droplet radius ranges from 1 μm to about 300 μm. The effective radius of the cumulus cloud droplet distribution without the precipitation mode is 6.0 μm. The cumulus cloud is represented by the first mode of the distribution, the drizzle droplets by the second mode. The drizzle droplet concentration is approximately five orders of magnitude lower and much wider than the one of the cloud mode.

The spectral power (red curve) is as well illustrated in Figure 20. It is seen that the spectral power is represented by two separated modes. The first mode is produced by the cloud droplets of the size distribution and has its maximum at a droplet radius of about 8 μm. The second mode, two orders of magnitude larger than the first one, is produced by the drizzle droplet size distribution and has its maximum at about 110 μm droplet radius. The five-orders-of-magnitude larger maximum in the cloud droplet size distribution of the cumulus mode produce a much lower maximum in the power spectrum of about -40 dBZ μm^{-1}, whereas the one produced by the peak concentration of the drizzle droplets is -25 dBZ μm^{-1}. This

Table 3: Parameters for the calculation of a droplet size distribution of a cumulus cloud [*Deirmendjian*, 1969] after Equation 4.30, and of the droplet size distribution for a precipitation mode [*Van Zanten et al.*, 2005] after Equation 4.32.

[*Deirmendjian*, 1969]	A_w	α_w	B_w [μm^{-1}]	Γ_w
Cumulus cloud droplet size distribution	2.373	6	1.50	1
[*Van Zanten et al.*, 2005]	N_0	σ_g	D_g[μm]	
Droplet size distribution for precipitation	0.033	1.55	86	

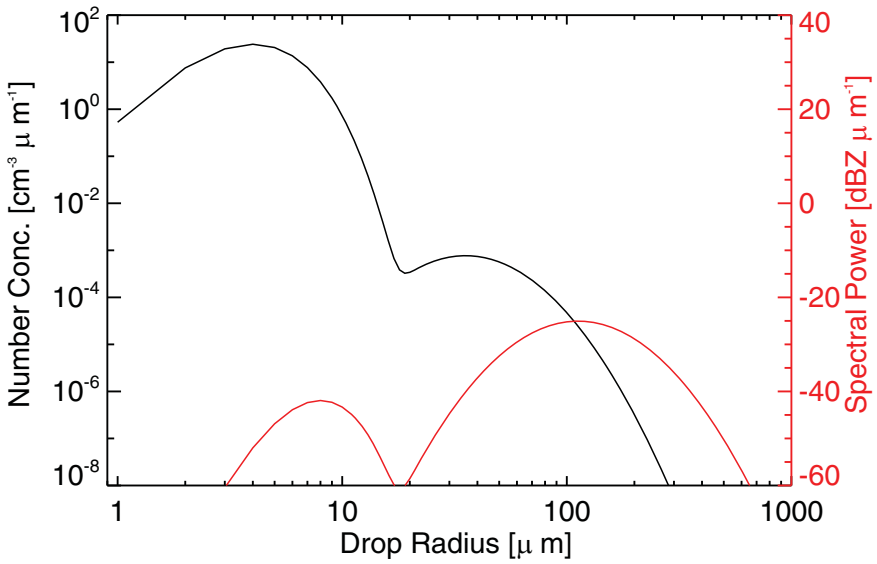

Figure 20: Simulated droplet size distribution (black curve) and power spectrum (red curve) of a drizzling cumulus cloud as a function of the droplet radius.

is again due to the D^6-dependency of the reflectivity (Equation 2.14) which is also the reason for the shifts of the maxima of the power spectrum to larger droplet radii compared to the one of the droplet size distribution. The total calculated reflectivity of the size distribution is -3.727 dBZ and the calculated liquid water content of the total droplet size distribution is 0.089 $\mathrm{g\,m^{-3}}$.

The simulated Doppler spectrum (red curve) and the droplet number concentration (black curve) for the drizzling cumulus cloud are illustrated in Figure 21. The mean Doppler velocity of the spectrum is -0.184 $\mathrm{m\,s^{-1}}$ and was calculated from the Doppler spectrum with Equation 2.19.

The Doppler spectrum shows two maxima as expected from theory in Chapter 2.5 and the measurement example in Chapter 3.5. Seen is that the drizzle droplet mode dominates the spectrum. The first maximum derived for the cloud droplet mode at about -0.02 $\mathrm{m\,s^{-1}}$ is 20 $\mathrm{dBZ\,m^{-1}\,s}$ lower than the second maximum of the drizzle mode at about -0.25 $\mathrm{m\,s^{-1}}$. It can be seen again that the velocity range of the Doppler spectrum is wider than the droplet size distribution and ranges from 0 $\mathrm{m\,s^{-1}}$ to about -1.1 $\mathrm{m\,s^{-1}}$.

As for the stratus-cloud case presented in the previous section, the actual spectrum of the cloud-mode of the drizzling cumulus would be detected as a single peak in the Doppler spectrum of MIRA-35. This is due to the Doppler-velocity resolution of MIRA-35 which is 8 $\mathrm{cm\,s^{-1}}$.

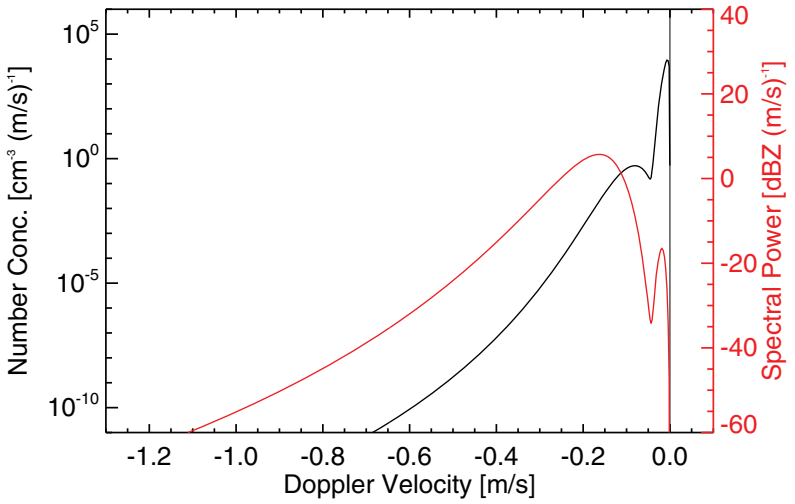

Figure 21: Simulated droplet size distribution (black curve) and Doppler spectrum (red curve) of a drizzling cumulus cloud as a function of the Doppler velocity.

5 Determinitation of microphysical properties of drizzle and clouds

So far this thesis dealt with the theoretical relationship between radar signal and cloud or drizzle microphysical properties. In the following Chapter it is shown how the background given in the previous chapters can be applied to remote sensing measurements.

Existing schemes for the retrieval of cloud and drizzle microphysical properties have in common that the goal is to determine the parameters that are needed to describe analytical droplet size distributions. In the scope of this thesis, one of such retrieval schemes, based on *Frisch et al.* [1995], was implemented at TROPOS. The method of *Frisch et al.* [1995], in the following denoted Frisch-method, allows for the retrieval of both drizzle and cloud droplet microphysical properties. It is based solely on radar measurements of the Doppler velocity, Doppler spectral width, and reflectivity. The Frisch-based concepts for the retrieval of drizzle microphysical properties and of cloud droplet microphysical properties are presented in Section 5.1 and Section 5.2, respectively.

In Section 5.3 an independent approach of *O'Connor et al.* [2005] for the determination of drizzle droplet microphysical properties is presented. Herein, it will only be used for comparison with the results obtained with the Frisch-method. The retrieval of *O'Connor et al.* [2005] differs from the one of *Frisch et al.* [1995] because it does not rely on the radar measurement of the Doppler velocity. Instead, it uses Ceilometer measurements of cloud optical extinction as an additional constraint.

5.1 Determination of drizzle microphysical properties with radar

In this Section the method provided by *Frisch et al.* [1995] to determine microphysical properties of drizzle droplets is introduced. The Frisch-method is based on the determination of parameters that are needed to solve a logarithmic normal distribution $n(x)$ [*Davidson et al.*, 1984]

$$n(x) = \frac{N}{\sigma_{\mathrm{x}}\sqrt{2\pi}} \exp\left\{-\frac{(x-x_0)^2}{2\sigma_{\mathrm{x}}^2}\right\} \tag{5.33}$$

that describes the number size distribution of either drizzle droplets or cloud droplets. In Equation 5.33, N is the total droplet number concentration per unit volume, σ_{x} the logarithmic width of the distribution, $x_0 = \ln(r_0)$ describes the mean droplet radius r_0 in μm, and $x = \ln(r)$ is the logarithm of the droplet radius.

To calculate the microphysical droplet properties Frisch used the moments of the

logarithmic normal distribution

$$\left\langle r^k \right\rangle = N^{-1} \int_0^\infty r^k n(r) \mathrm{d}r = r_0^k \cdot \exp\left\{ \frac{k^2 \sigma_\mathrm{x}}{2} \right\} \tag{5.34}$$

where $\left\langle r^k \right\rangle$ is the kth moment of the logarithmic normal distribution $n(r)$ that now depends directly on the radius after setting $r = e^x$. To determine microphysical droplet properties using radar-data the three parameters that solve the logarithmic normal distribution (r_0, σ_x, and N) must be obtained.

The reflectivity Z (see Equation 2.14) can derived from the logarithmic normal distribution using Equation 5.34:

$$Z = 2^6 N \left\langle r^6 \right\rangle = 2^6 N r_0^6 \exp\left\{ 18 \sigma_\mathrm{x}^2 \right\} \tag{5.35}$$

For the calculations in *Frisch et al.* [1995] the reflectivity Z is expressed in units of m^3 instead of $\frac{mm^6}{m^3}$ that is usually provided from radar measurements.

As shown by *Frisch et al.* [1995] the Doppler-velocity spectrum $\left\langle V^k \right\rangle_D$ can also be derived from the moments of the logarithmic normal distribution:

$$\left\langle V^k \right\rangle_D = \frac{\left\langle r^6 \left[V_\mathrm{f}(r) \right]^k \right\rangle}{\left\langle r^6 \right\rangle} \tag{5.36}$$

In Equation 5.36 $\langle r^6 \rangle$ is the sixth moment of the logarithmic normal distribution and $V_\mathrm{f}(r)$ the radius-dependent fall velocity of the droplet.

To derive the Doppler spectrum, *Frisch et al.* [1995] used a fall-velocity approximation because fall velocity $V_\mathrm{f}(r)$ depends on the droplet size. The approximation relates the droplet fall velocity linear to the droplet radius [*Gossard et al.*, 1990]:

$$r = a V_\mathrm{f}(r) + b \tag{5.37}$$

In Equation 5.37 $a = 1.2 \cdot 10^{-4}\,\mathrm{s}$ and $b = 1 \cdot 10^{-5}\,\mathrm{m}$. The approximation is only valid for droplets with a radius between 45 μm and 400 μm and a fall velocity $V_\mathrm{f}(r)$ between 0.3 $\mathrm{m\,s^{-1}}$ and 3.0 $\mathrm{m\,s^{-1}}$. Thus all droplets with $r > 45$ μm are declared as cloud droplets and droplets with $r < 400$ μm are declared as rain droplets. The parametrisation is illustrated in Figure 22. In comparison to the one presented in Equation 4.28 of Section 4.2 (illustrated in Figure 17) the range of validity for both the radius and the velocity is smaller. However, the parametrized fall velocities used in the Frisch-method are larger than the ones obtained with Equation 4.28. For $r = 45$ μm and $r = 400$ μm, Equation 5.37 yields, $v = 0.3$ $\mathrm{m\,s^{-1}}$ and $v = 3.0$ $\mathrm{m\,s^{-1}}$, respectively. For the same two readii, Equation 4.28 yields, $v = 0.09$ $\mathrm{m\,s^{-1}}$ and $v = 0.5$ $\mathrm{m\,s^{-1}}$, respectively. The discrepancies between the two parametrisations are

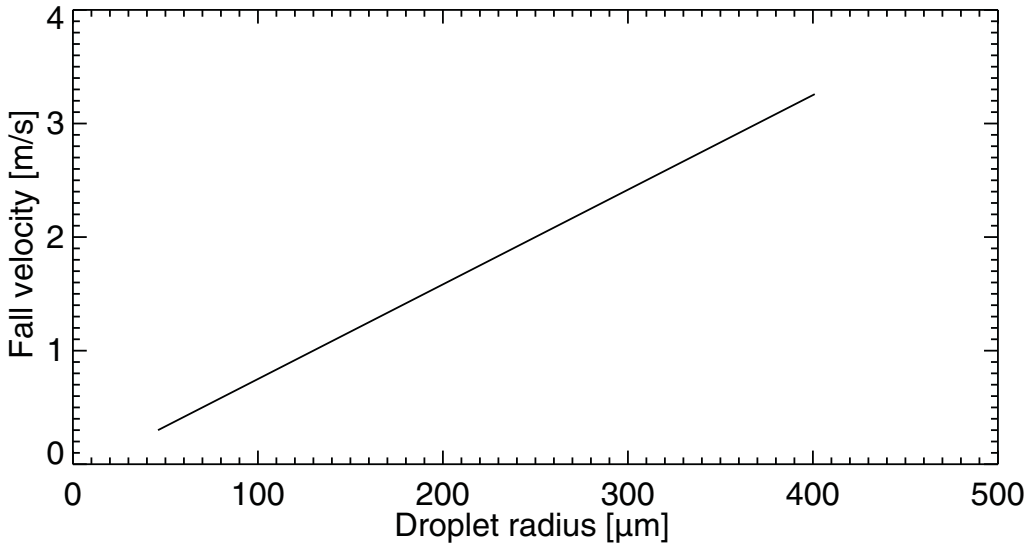

Figure 22: Relationship between droplet radius and fall velocity after *Gossard et al.* [1990] as applied in *Frisch et al.* [1995] and described by Equation 5.37.

remarkable. They are probably a result of the different approaches of *Beard* [1985] and *Gossard et al.* [1990] to establish the parametrisations. In the scope of this thesis the discrepancies were not studied in detail.

Frisch used the velocity approximation in Equation 5.37 to derive the mean Doppler velocity $\langle V \rangle_D$ from the first moment of Equation 5.36.

$$a \langle V \rangle_D + b = r_0 \cdot \exp\left\{\frac{13\sigma_{\mathrm{x}}^2}{2}\right\} \tag{5.38}$$

In Equation 5.38 the radar-measured Doppler velocity is a function of the mean radius r_0 and of the logarithmic width σ_x of the logarithmic normal distribution.

Frisch derives the Doppler width σ_{v} from the logarithmic normal distribution as shown in Equation 2.20:

$$\sigma_{\mathrm{v}}^2 = \left\langle V^2 \right\rangle_{\mathrm{D}} - \left(\langle V \rangle_{\mathrm{D}}\right)^2 = \left(\frac{r_0}{a}\right)^2 \exp\left\{13\sigma_{\mathrm{x}}^2\right\}\left[\exp\left\{\sigma_{\mathrm{x}}^2\right\} - 1\right] \tag{5.39}$$

In Equation 5.39 the measured Doppler width σ_{v} is again a function of the mean droplet radius r_0 and the logarithmic width of the logarithmic normal distribution. The combination of Equation 5.38 and Equation 5.39 yields an equation for the logarithmic width σ_{x} that depends only on radar-measured parameters:

$$\sigma_{\mathrm{x}} = \left[\log\left(1 + \frac{\sigma_{\mathrm{v}}^2}{\left(\langle V \rangle_{\mathrm{D}} + \frac{b}{a}\right)^2}\right)\right]^{\frac{1}{2}} \approx \frac{\sigma_{\mathrm{v}}}{\langle V \rangle_{\mathrm{D}}} \tag{5.40}$$

In Equation 5.40 only the radar-measured Doppler width σ_{v}, the Doppler velocity $\langle V \rangle_{\mathrm{D}}$, as well as the constants a and b are needed to calculate the logarithmic

width. Inserting Equation 5.40 into Equation 5.37 allows to calculate the mean droplet radius r_0 from radar data.

$$r_0 = [a \langle V \rangle_D + b] \exp\left\{-\frac{13\sigma_x^2}{2}\right\} \tag{5.41}$$

The combination of the transformed Equations 5.35, 5.40, and 5.41 yields an equation for the total droplet number concentration N that then also depends only on parameters measured with radar.

$$N = \frac{Z}{2^6 r_0^6 \exp\{18\sigma_x^2\}} \tag{5.42}$$

The set of Equations 5.40, 5.41, and 5.42 is the key to convert the radar-measured parameters σ_v, $\langle V \rangle_D$, and Z to the input parameters σ_x, r_0, and N of the logarithmic normal distribution.

Another microphysical droplet property *Frisch et al.* [1995] derived from the logarithmic normal distribution is the liquid water content q_l.

$$q_l = \frac{4}{3}\pi \cdot \rho_w N \cdot \left\langle r^3 \right\rangle = \frac{4}{3}\pi \rho_w N r_0^3 \exp\left\{\frac{9\sigma_x^2}{2}\right\} \tag{5.43}$$

5.2 Determination of cloud microphysical properties with radar and microwave radiometer

In the same paper *Frisch et al.* [1995] provided an approach to calculate the liquid water content of cloud droplets. Replacing the mean radius r_0 in Equation 5.35 with the one from the transformed Equation 5.43 yields

$$q_l = \frac{\pi}{6} \exp\left\{-\frac{9}{2}\sigma_x^2\right\} \rho_w Z^{\frac{1}{2}} N^{\frac{1}{2}}. \tag{5.44}$$

With Equation 5.44 the liquid water content of cloud droplets can be calculated from the measured reflectivity and Doppler width. The total number of the cloud droplets N needs to be varied in such a way that a known value of q_l is obtained. In the paper the value of the logarithmic width σ_x is thus set constant to 0.35 [*Frisch et al.*, 1995]. So the equation can be given as:

$$q_l = 0.30 \rho_w Z^{\frac{1}{2}} N^{\frac{1}{2}} \tag{5.45}$$

To get an impression about the accuracy of the liquid water content, Equation 5.45 was tested against values of q_l provided by *Miles et al.* [2000]. From the droplet size distribution given in *Miles et al.* [2000] the reflectivity is calculated with Equation 4.24. The calculated reflectivity Z as well as the total number concentration N of the droplets are then applied to derive q_l with Equation 5.44. Table 4 displays

Table 4: Test of the validity of the assumption that $\sigma_x = 0.35$ in Equation 5.45 by comparing the calculated liquid water content q_l^{cal} to the reference value q_l^{ref} from *Miles et al.* [2000]. Reflectivity Z and droplet number concentration N needed to solve Equation 5.45 were taken from *Miles et al.* [2000]. Δq_l is the discrepancy between q_l^{ref} and q_l^{cal}. σ_x^{ref} is the logarithmic width obtained from Equation 5.44 for N, Z, and q_l^{ref} from *Miles et al.* [2000].

Reference in paper	N [cm^{-3}]	Z [dBZ]	q_l^{ref} [g m^{-3}]	q_l^{cal} [g m^{-3}]	Δq_l	σ_x^{ref}
[*Martin et al.*, 1994]	160	-42.640	0.03	0.028	7 %	0.33
[*Hayasaka et al.*, 1995]	148	-20.595	0.40	0.34	15 %	0.34
[*Slingo et al.*, 1982]	680	-42.650	0.08	0.058	27 %	0.22

the measured liquid water content q_l^{ref} of *Miles et al.* [2000] and the calculated liquid water content (q_l^{cal}) after Equation 5.43 in the fourth and in the fifth column, respectively. Overall, the q_l calculated after Equation 5.44 with $\sigma_x = 0.35$ is lower than the measured ones. Discrepancies $\Delta q_l = \frac{|q_l^{cal} - q_l^{ref}|}{q_l^{ref}} \cdot 100$ range from 7-28%. The column σ_x^{ref} shows the logarithmic width calculated with Equation 5.44 for Z, N, and q_l taken from *Miles et al.* [2000].

From Equation 5.44 it can be seen that q_l must be known in order to derive the cloud droplet number concentration from the measured reflectivity. According to *Frisch et al.* [1995] this fact can be overcome by taking the microwave-radiometer measurements of the LWP into account. Assuming that N is constant at all heights in a cloud layer, the layer-integral of q_l should yield the measured LWP W_p

$$W_p = \int_{H_{base}}^{H_{top}} q_l(h)\mathrm{d}h = 0.30\rho_w N^{\frac{1}{2}} \int_{H_{base}}^{H_{top}} Z(h)^{\frac{1}{2}}\mathrm{d}h \tag{5.46}$$

Equation 5.46 can be rearranged to obtain N:

$$N = \left(\frac{W_p}{0.30\rho_w \int_{H_{base}}^{H_{top}} Z(h)^{\frac{1}{2}}\mathrm{d}h} \right)^2 \tag{5.47}$$

Even though this thesis concentrates on the retrieval of drizzle microphysical properties, the applicability of Equation 5.47 is briefly checked in the following paragraph by means of a case study. In Figure 23 a cloud-radar measurement of 12 May 2012, 1315 – 1345 UTC, is illustrated. From the equivalent reflectivity of hydrometeors (Figure 23 (a)) it can be seen that cloud layers were present at around 2.0-km height throughout the observation time. The Doppler velocity observed in the cloud layers (see Figure 23 (b)) alternates between up- and downdrafts over a range from -1 to $+2$ m s^{-1}. The small cloud droplets are driven by atmospheric turbulent motions that dominate the droplet terminal velocity. Thus, a relationship

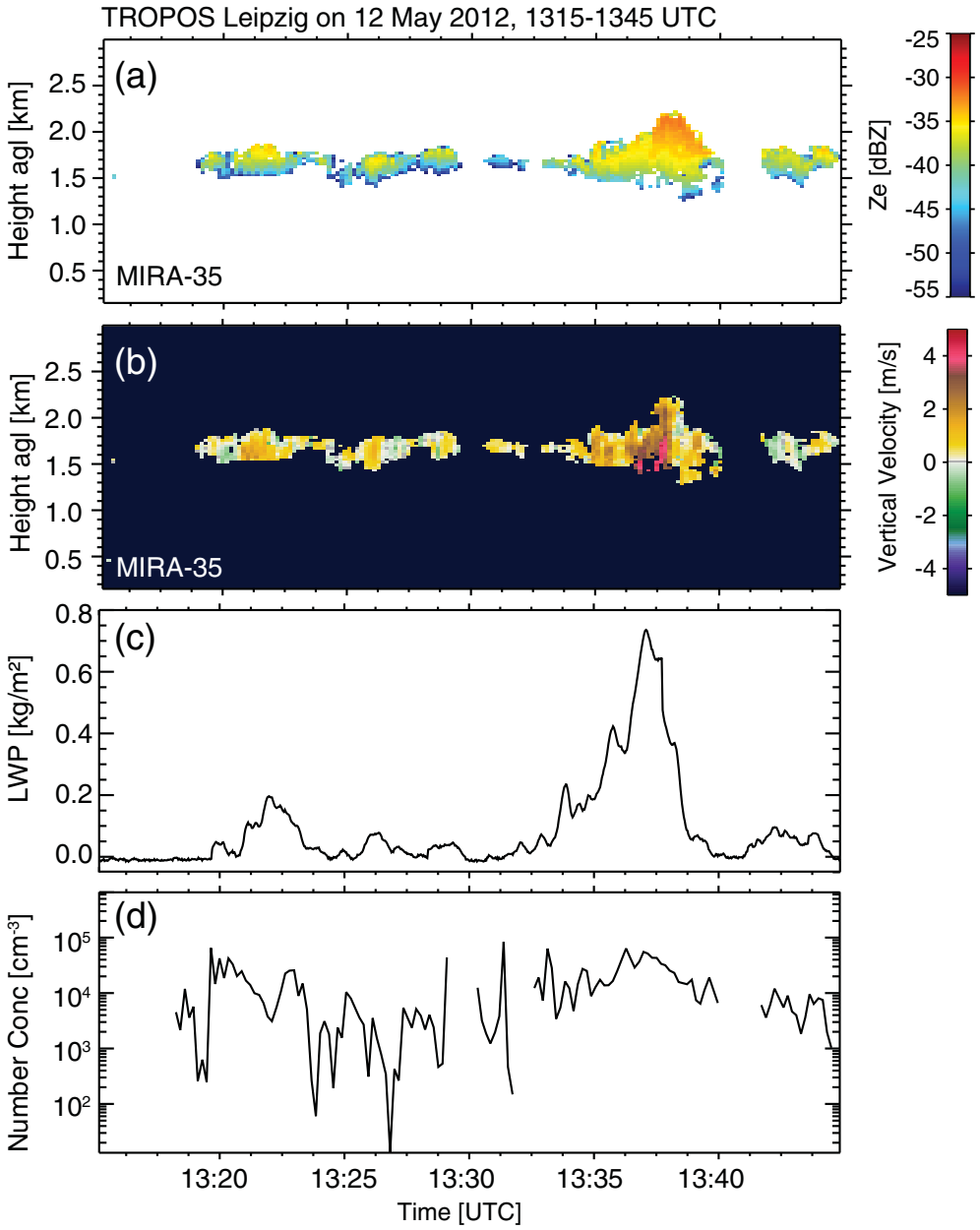

Figure 23: Measurement of a cumulus cloud field on 12 May 2012, 1315–1345 UTC, at TROPOS. (a) and (b) show observations of the equivalent reflectivity of hydrometeors and the Doppler velocity, respectively, performed with MIRA-35. In (c) the LWP measured with HATPRO is illustrated, and in (d) the cloud droplet number concentration obtained after Equation 5.47 is presented.

between the size and the fall velocity of the droplets cannot be applied to estimate the cloud droplet size. This is the reason, in addition to the too-low Doppler-velocity resolution of MIRA-35 (see Section 3.1), why the approach of *Frisch et al.* [1995] to derive drizzle microphysical properties cannot be used to study cloud droplets.

Figure 23 (c) shows the LWP measured with HATPRO (see Section 3.3). The gaps in the measurement are caused by interruptions of the measurement of the microwave radiometer during calibration periods or elevation scans.

Table 5: Droplet number concentration N calculated after Equation 5.47 from the LWP W_{p} measured with HATPRO and the reflectivity Z measured with MIRA-35 for selected times of the measurement performed on 12 May 2012 that is introduced in Figure 23.

Time [UTC]	LWP [kg m^{-2}]	Z dBZe	N [cm^{-3}]
13:34:14	0.062	-37.40	9500
13:34:44	0.12	-40.14	46000
13:35:14	0.13	-37.91	6190
13:35:45	0.20	-37.36	16700
13:36:15	0.28	-37.21	26200
13:36:45	0.37	-37.00	37500
13:37:15	0.49	-35.29	61750
13:37:44	0.72	-34.56	32100

In Figure 23 (d) the droplet number concentration N obtained after Equation 5.47 is presented. In Table 5 some calculated droplet number concentrations are shown, too. The derived values of N vary strongly over several orders of magnitude. In most cases droplet number concentrations larger than 10000 cm^{-3} were calculated. According to *Miles et al.* [2000] typical values of N are in the order of 100 to 500 cm^{-3}.

In conclusion, the approach of *Frisch et al.* [1995] for the estimation of the cloud droplet number concentration does not seem to be applicable to ambient clouds. The assumptions of a fixed logarithmic width σ_{x} and a height-constant droplet number concentration N are probably large sources of uncertainties.

5.3 Determination of drizzle microphysical properties with radar and lidar

To allow for the estimation of the applicability of the Frisch-method a second approach of *O'Connor et al.* [2005] for the detection of drizzle microphysical properties is presented in the following Section.

The method of *O'Connor et al.* [2005] is based on combined measurements of lidar and cloud radar. Already *Intrieri et al.* [1993] showed, that the ratio between lidar-backscattered power and radar-backscattered power is a sensitive function of the mean droplet size.

The approach of *O'Connor et al.* [2005] is based on three prerequisites. First, the drizzle droplet distribution follows a normalized gamma distribution:

$$n(D) = N_{\mathrm{W}} \frac{6}{3.67^4} \frac{(3.67+\mu)^4}{\Gamma(\mu+4)} \left(\frac{D}{D_0}\right)^{\mu} \exp\left\{\frac{-(3.67+\mu)D}{D_0}\right\} \tag{5.48}$$

Equation 5.48 is parametrized via the normalized total droplet number concentration

N_W, the shape parameter μ, and the median equivolumetric diameter D_0.

Second, the drizzle droplets must be much larger than the wavelength at witch the lidar is operated. In that case the lidar-measured optical extinction α can be expressed by

$$\alpha = \frac{\pi}{2} \int_0^\infty n(D)\, D^2\, dD = S_l \beta. \tag{5.49}$$

With Equation 5.49 the relationship between α and backscatter coefficient β can be described by the lidar ratio S_l.

Third, the radar reflectivity Z can be expressed by

$$Z = \frac{|K_\mathrm{T}|}{|K_0|} \int_0^\infty n(D)\, D^6\, \gamma(D)\, \mathrm{d}D \tag{5.50}$$

where $|K_\mathrm{T}|$ is the dielectric factor of water at a temperature T, $|K_0|$ is the dielectric factor of liquid water at 0 °C, and $\gamma(D)$ is the Mie/Rayleigh backscatter ratio. The backscattered radar signal has a small contribution of Mie-scattered signal so $\gamma(D)$ had to be considered in Equation 5.50.

In order to get rid of the dependence on $n(D)$ *O'Connor et al.* [2005] calculate the ratio between Equations 5.50 and 5.49:

$$\frac{Z}{\alpha} = \frac{2}{\pi} \frac{\Gamma(7+\mu)}{\Gamma(3+\mu)} \frac{S(D_0,\mu)\gamma'(D_0,\mu)}{(3.67+\mu)^4} D_0^4 \tag{5.51}$$

This ratio is the base for the calculation of the mean diameter D_0. For the calculation of D_0 the dependency of the lidar ratio $S(D_0,\mu)$ and the Mie/Rayleigh backscatter ratio $\gamma'(D_0,\mu)$ on the shape of the distribution μ and on D_0 need to be known. These relationships are given by *Van de Hulst* [1957] for the Mie/Rayleigh backscattering ratio, and by *O'Connor et al.* [2005] for the lidar ratio.

To derive μ and D_0 from Equation 5.51, an iterative approach is applied. The first guess of the mean radius D_0 can by found by assuming the shape parameter of the distribution $\mu = 0$. To get the right shape parameter for the distribution the measured spectral width is compared to the respective one calculated after

$$\sigma_\mathrm{d}^2 = \frac{\int_0^\infty (v(D) - V)^2\, n(D)\, D^6\, \gamma(D)\, dD}{\int_0^\infty n(D)\, D^6\, dD}. \tag{5.52}$$

Equation 5.52 is similar to Equations 2.20 and 4.24 but *O'Connor et al.* [2005] use an extended version that accounts for Mie-scattering by means of $\gamma(D_0,\mu)$. In Equation 5.52 $v(D)$ is the terminal velocity of a droplet with diameter D and V is the mean Doppler velocity.

Iteratively the mean diameter D_0 is fitted using Equations 5.51 and 5.52. Once D_0

and μ are found, the third parameter N_{W} is derived from the observed reflectivity Z. Now the size distribution (Equation 5.48) can be calculated with the derived parameters. The calculated size distribution is used, e.g., to calculate the drizzle liquid water content q_{d}:

$$q_{\mathrm{d}} = \rho_{\mathrm{w}} \frac{\pi}{6} \int_0^\infty n(D)\, D^3\, dD \tag{5.53}$$

In Chapter 6.1 the drizzle microphysical properties derived after *O'Connor et al.* [2005] will be put into context with the values obtained with the Frisch-method.

6 Calculation of microphysical drizzle properties

In this Chapter the determination of microphysical properties of drizzle droplets are illustrated. The results were produced by the method that was provided in *Frisch et al.* [1995]. This is done by means of two case studies that are presented in Sections 6.2 and 6.3. First, the preprocessing scheme for the radar data is introduced in Section 6.1 It is explained how the original data products of the cloud radar are processed in order to obtain only data points that can be attributed to drizzle droplets. Section 6.2 then presents a case study of a single short-lived precipitation cell whereas Section 6.3 presents one of a drizzling stratus cloud.

6.1 Preprocessing of data

The applicability of the Frisch-method is based on four basic requirements:

1. Only warm-rain processes are involved in the precipitation formation.
2. Large rain drops are absent.
3. The range of validity of the diameter-velocity relationship (Equation 5.38) used by *Frisch et al.* [1995] must be hold.
4. The contribution of cloud droplets to the measured reflectivities and Doppler spectra are negligible.

The reflectivity Z of hydrometeors can only be accurately determined for spherical liquid water droplets. When non-spherical ice crystals are present, Equation 2.15 is not valid anymore. Item 1 of the list above was thus ensured by checking the studied clouds for their minimum temperatures. For this purpose, temperature profiles of numerical weather models for the model gridpoint nearest to TROPOS were used. When the minimum temperature of the cloud was above 0 °C, ice cannot be formed. It is well known that even so-called supercooled cloud layers with temperatures between 0 °C and −40 °C may form ice-free precipitation (e.g., *Seifert et al.* [2010]). When precipitation falling out of such supercooled cloud layers passes the height level where $T = 0\,°\mathrm{C}$, the radar measurement of the reflectivity and of the depolarization ratio may be used for the identification of the phase state of the precipitation. Melting ice crystals produce the so-called radar bright-band [*Szyrmer and Zawadzki*, 1999] that is characterized by increased reflectivity and high depolarization ratio. When a bright band is absent, the precipitation is pure liquid. In the case of precipitation that only occurs at temperatures below 0 °C, radar alone cannot be used straight-forward to determine the phase state of the precipitation.

Item 2 of the list of requirements is important because the approach of Frisch does not take the attenuation of the radar signal by Mie scattering into account. Hence,

the observed droplets must be small in order to stay in the range of validity of the Rayleigh approximation. In the scope ot this thesis only clouds were analysed that did not produce detectable amounts of precipitation at the ground. The precipitation droplets observed during the case studies are thus assumed to be small enough to evaporate before they could reach the ground.

Item 3 must be accounted for because the range of validity of the diameter-velocity relationship introduced in Equation 5.36 spans only from -0.3 to $-3\,\mathrm{m\,s^{-1}}$. Data points showing smaller or larger fall velocities must be excluded before the determination of drizzle droplet microphysical properties.

Item 4 is based on the fact that in real clouds atmospheric motions superimpose the fall velocity of the cloud and precipitation droplets. When atmospheric downdrafts are present, even small cloud droplets may show apparent fall velocities that are in the range of validity after Item 3 above. To remove false-positive misclassification of cloud droplets as drizzle droplets a reflectivity threshold was applied in addition. Hence, only data points that produced reflectivities of above -15 dBZ were used for analysis. As was shown in Figure 7 and in Chapter 4, clouds usually produce reflectivities that are below -20 dBZ. Higher reflectivities can only be produced by larger drizzle-sized droplets.

In Figure 24 it is illustrated in a case study how the data are filtered before the microphysical properties of drizzle droplets are calculated with the Frisch-method. Figure 24 (a) presents a time-height cross section of the reflectivity observed between 0615 and 0635 UTC on 14 August 2011. The cloud extends from close to the ground to approximately 1.4 km. The reflectivity ranges between -40 and 5 dBZ. Temperatures on that day were above 0 °C up to heights of 4 km. Thus, the occurrence of ice can be excluded. According to ground-based measurements of rain gauge and optical disdrometer no rain reached the ground. Large rain drops were such likely to be absent during the measurement.

Figure 24 (b) presents an additional filtering step during which all profiles were removed from the data set for which no microwave-radiometer observation of the liquid water path was available. Such gaps occur when the microwave radiometer performs auto-calibrations.

Figure 24 (c) shows the measured Doppler velocity of the hydrometeors. It can be seen that the velocity is in part larger than $-0.3\,\mathrm{m\,s^{-1}}$. Such data points as well as the ones that showed reflectivities of below -15 dBZ were removed from the full data set.

The resulting data set that contains only valid data points for the application of the Frisch-method is shown in Figure 24 (d).

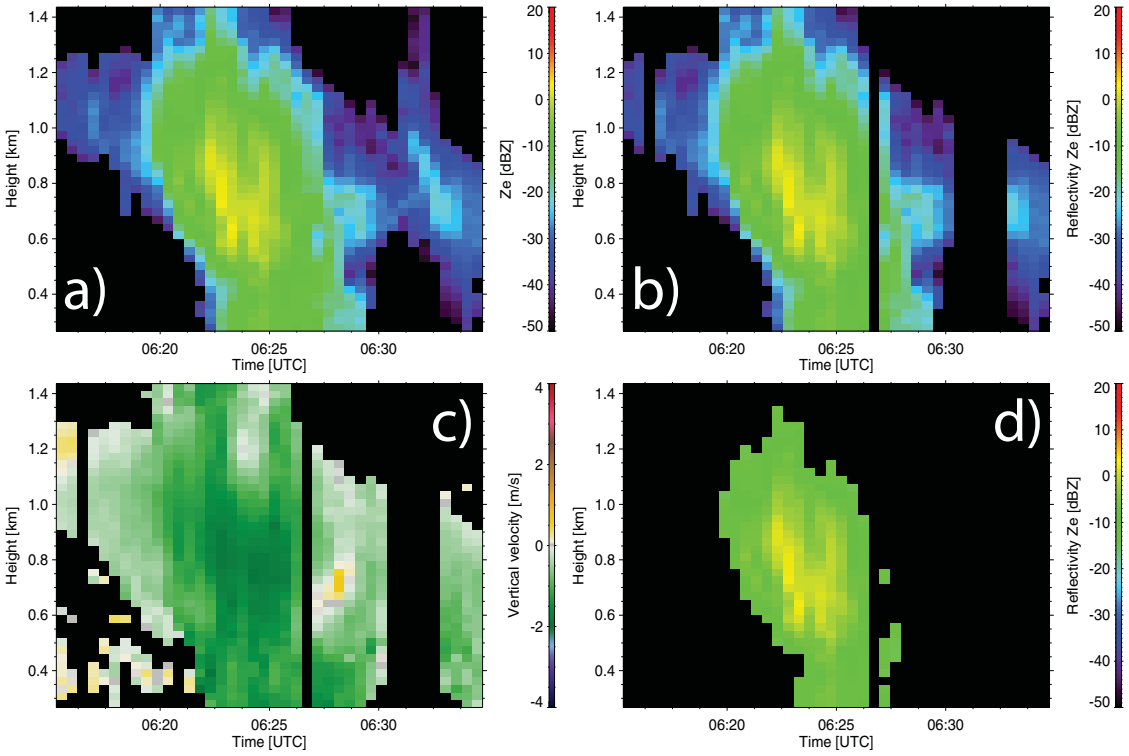

Figure 24: Demonstration of preprocessing of reflectivity Z_e and Doppler velocity before the Frisch-method can be applied. Shown is a measurement of 14th August 2011, 0615–0635 UTC. Figure (a) shows the effective reflectivity Ze of water droplets measured with MIRA-35, (b) shows only the data points where LWP of HATPRO were available, (c) shows the Doppler velocity of all hydrometeors measured with MIRA-35, and (d) shows the reflectivity for the data points that remained after the preprocessing.

6.2 Single precipitating cloud cell on 14 August 2011

In this Section the results of the Frisch-method for a single precipitating cloud cell that was observed at TROPOS on 14 August 2011, 0615 to 0635 UTC, is presented. The mean droplet radius r_0 was calculated with Equation 5.41, the total droplet number concentration N with Equation 5.42, and the liquid water content (LWC) q_l with Equation 5.44.

In Figure 25 the results of the microphysical property calculations are illustrated. In Figure 25 (a) the filtered reflectivity data in dBZ are shown. The vertical lines highlight the three time points for which profiles of droplet number concentration, droplet radius and liquid water content are shown in Figure 25 (b), (c), and (d), respectively. In the graphs, the white line corresponds to the position of the black line in Figure 25 (a).

In Figure 25 (b) the profiles of calculated droplet number concentration for the three time points are shown. The droplet number concentrations run over two orders of magnitude from 20 m^{-3} to 4000 m^{-3}. The slope of the three profiles is similar.

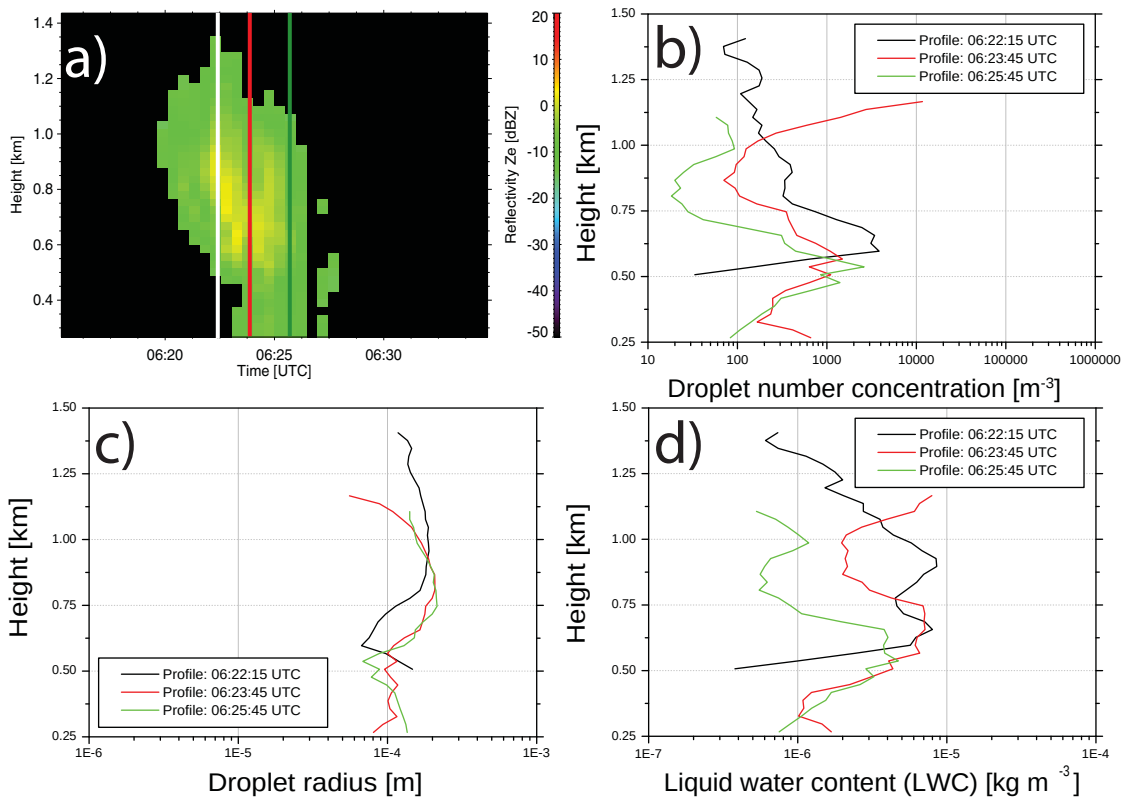

Figure 25: Drizzle microphysical properties of a single precipitating cloud cell on 14 August 2011, 0615–0635 UTC, as calculated with the Frisch-method. Figure (a) shows the preprocessed reflectivity. The vertical lines mark the three profiles (06:22:15 UTC: white, respectively black curve; 06:23:45 UTC: red curve; 06:25:45 UTC: green curve) for which results are shown in (b)–(d). (b) shows the calculated droplet number concentration, (c) shows the mean radius, and (d) the liquid water content.

All show a maxima between heights of 500 m and 750 m. The height of the maxima as well as the maximum droplet number concentration decrease with increasing time from 3800 m^{-3} at 600 m height at 06:22:15 UTC to values of below 2000 m^{-3} at around 550 m height at 06:23:45 and 06:25:45 UTC.

The mean droplet radius shown in Figure 25 (c) does only vary from 60 μm to 230 μm. The slope of the profiles of the mean radius is not correlated to the respective one of the droplet size distributions. The lowest radii are however found closer to the ground where also the droplet size distribution was found to be low.

The liquid water content of the drizzle illustrated in Figure 25 (d) is a function of the droplet size distribution and the mean radius. It is highest when the mean radius is large and the droplet number concentration is high. The liquid water content varies within one order of magnitude, reaching values between $7 \cdot 10^{-7}$ kg m^{-3} to $1 \cdot 10^{-5}$ kg m^{-3}.

Overall, the calculated radii fit well to the radii range of the simulated droplet size distribution of drizzle in Chapter 4.3.2 that was shown in Figure 20.

At heights below 1 km all retrieved parameters show a rather conclusive picture of the scenario. Probably an updraft in the actual cloud layer at above 1 km height initialized the formation of a drizzle cell. With time, the drizzle descends toward the ground. This is suggested by the slow descend of the maximum in the droplet number concentration shown in Figure 25 (b).

At heights above 1 km, the retrieved microphysical parameters vary strongly from profile to profile. Here, probably the radar measurement is already affected by the presence of small cloud droplets. Also, the measured reflectivity and velocity were low in the upper part of the drizzle cell. Atmospheric motion have a strong influence on the terminal velocity when the actual fall speed of the droplets is already low. The case study in the next Section 4.1 considers the cloud base measured with Ceilometer. The effect of atmospheric vertical motions on the retrieved drizzle microphysical properties is discussed in a case study in Chapter 7.

6.3 Drizzling stratus cloud on 10 September 2011

In this Section a second precipitation case is shown. The event was observed on 10 September 2011 from 0350 UTC to 0510 UTC. The microphysical properties were also calculated with the Frisch-method. In addition, the results are compared with the ones obtained after *O'Connor et al.* [2005].

In contrast to the case presented in Section 6.2, a long-lasting drizzle event is presented in this section. The observation is introduced in Figure 26. From 0350 to 0510 UTC continuously precipitation was observed with MIRA-35. The top of the precipitating cloud layer was at around 1800-m height, as the measurement of the reflectivity in Figure 26 (a) shows. Throughout the measurement, the reflectivity decreases with decreasing distance to the ground. This indicates that the precipitation did evaporate before it could reach the surface. This was also confirmed by the absence of precipitation in the measurements of the rain gauge and the optical disdrometer at TROPOS (not shown here).

The vertical velocity observed with MIRA-35 (see Figure 26 (b)) was predominantly negative during the measurement. Only at cloud top positive velocities were occasionally observed which indicates that cloud droplets driven by atmospheric motions dominated backscattering.

Figure 26 (c) presents the collocated measurement of the ceilometer. Shown is the so-called attenuated backscatter which is the calibrated raw signal measured with a lidar [*Weitkamp*, 2005]. The ceilometer measurement shows a different picture of the scenario. Most of the precipitation observed with MIRA-35 was also detected with the ceilometer. However, the signal was attenuated quickly at heights around 1200 m due to the presence of small cloud droplets. This is similar to the effects discussed in the case study presented in Section 2.1. The base of the actual cloud

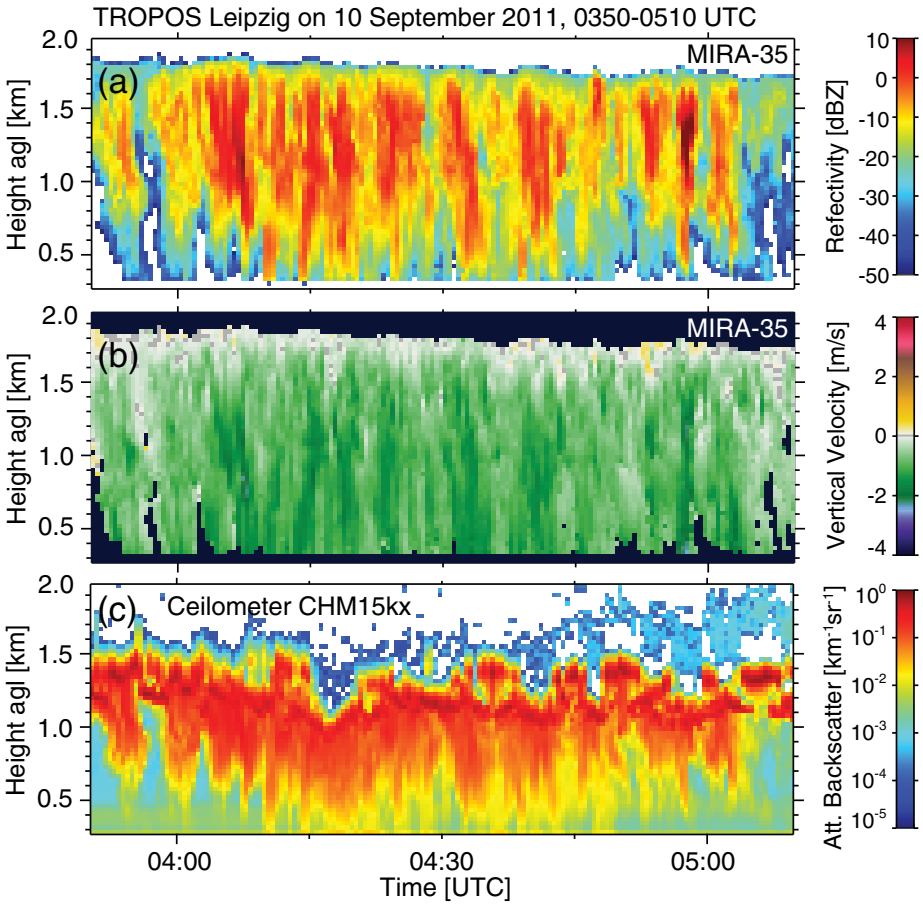

Figure 26: Radar and Ceilometer measurement of 10 September 2011, 0350 – 0510 UTC at TROPOS. a) show the with MIRA-35 measured reflectivity, b) displays the with MIRA-35 measured Doppler velocity, and c) illustrates attenuated backscatter which is the calibrated raw signal measured by the Ceilometer.

layer thus was located at heights of around 1200 m.

In Figure 27 (a) the reflectivity of water drops is illustrated after the data was preprocessed according to the scheme provided in Section 6.1. The four vertical lines highlight the four time points for which the profiles of microphysical properties are calculated. Figure 27 the profiles for 04:07:44 UTC, 04:18:45 UTC, 04:38:45 UTC, and 04:57:45 UTC are shown in black (white), red, blue, and green, respectively.

Figure 27 (b) shows the profiles of the drizzle droplet number concentration for the four times indicated in Figure 27 (a). The profiles are correlated well. In the upper part of the drizzling region above 1.25 km height, the variability of the drizzle droplet number concentration increases, similar as for the case presented in Section 4.1. Values of above 10^6 m^{-3} were calculated with the Frisch-method. Such values (corresponding to 1 droplet per cm^{-3}) are already in the range of cloud droplet number concentrations that were observed to be as low as 50 cm^{-3} [*Miles et al.*, 2000]. As indicated in the Ceilometer measurement shown in Figure 26 (c), the backscatter signal increased strongly already at heights of above 1100 m indicating the presence of the cloud base. The drizzle droplet number concentration at the

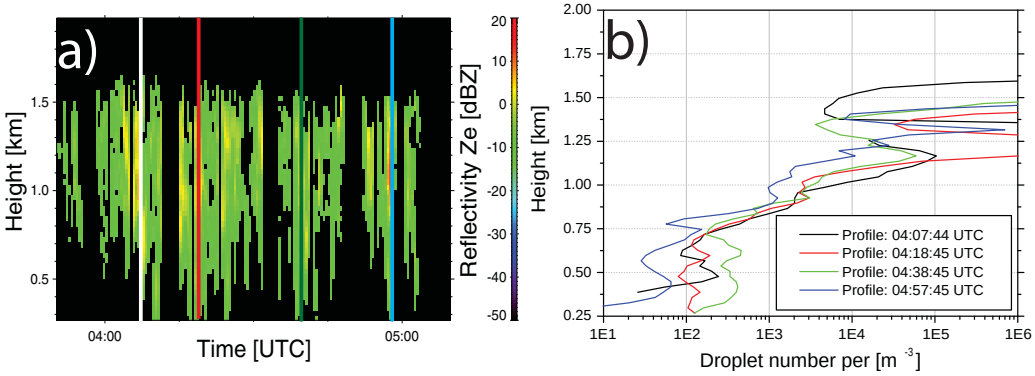

Figure 27: Drizzle microphysical properties of a drizzling stratus cloud observed on 10 September 2011, 0350–0510 UTC, as calculated with the Frisch-method. Figure (a) shows the preprocessed reflectivity. The vertical lines mark the four profiles (04:07:44 UTC: white, respectively black curve; 04:18:45 UTC: red curve; 04:38:45 UTC: green curve; 04:57:45 UTC: blue curve) for which results are shown in (b). (b) shows the calculated droplet number concentration.

bottom of the profiles, in turn, tends to very low values of less than 100 m^{-3}. This confirms that the drizzle actually evaporated with decreasing distance to the ground.

Figure 28 presents the remaining microphysical parameters of the droplet mean radius and liquid water content as derived with the Frisch-method and the method of *O'Connor et al.* [2005].

The results for the liquid-water-content calculations of *Frisch et al.* [1995] and *O'Connor et al.* [2005] are presented in Figure 28 (a) and (b), respectively. Even though the profiles of the liquid water content have similar shapes, the results of the method of O'Connor (see Figure 28 (b)) are one order of magnitude larger than the results calculated with the Frisch-method (shown in Figure 28 (a)). The liquid water content calculated with the O'Connor-method ranges between 0.01 $g\,m^{-3}$ at the bottom and 0.03 $g\,m^{-3}$ at the top. In the black profile, at 04:07:44 UTC, the highest LWC with a maximum of 0.095 $g\,m^{-3}$ is given at a height of 840 m.

The maximum LWC retrieved after Frisch is 0.01 $g\,m^{-3}$. It can be seen that the LWC increases with height, especially at heights above the Ceilometer-detected mean cloud base. In this region the radar measurements of reflectivity and fall velocity are obviously dominated by cloud droplets and atmospheric motions that produce an apparently higher liquid water content.

In Figure 28 (c) and (d) the mean-droplet-radius profiles obtained with the methods of Frisch and O'Connor, respectively, are illustrated. Again the mean radius varies strongly in the top region of the profiles calculated with the Frisch-method. This is again caused by the contribution of cloud droplets and atmospheric motions to the radar measurement. At heights below cloud base as indicated in the profiles of O'Connor, the mean radius is rather constant for both methods. However, quantitatively both methods yield mean radii that differ by a factor of about two to

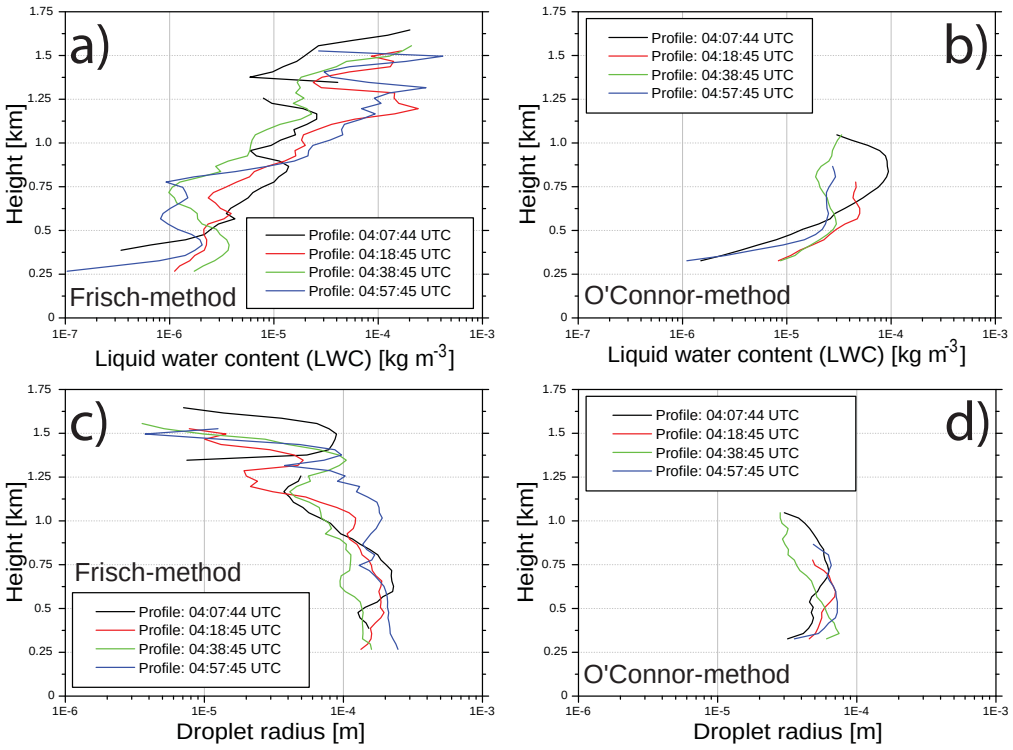

Figure 28: Comparison of microphysical drizzle properties obtained with the Frisch-method and the O'Connor-method for four time points during the observation of a drizzling stratus cloud on 10 September 2011 introduced in Figure 26. (a) and (b) show the liquid water content obtained with the Frisch-method and the O'Connor-method, respectively. (c) and (d) show the mean droplet radius obtained with the Frisch-method and the O'Connor-method, respectively.

four. Between 250 m and 1000 m above ground the mean radius retrieved with the Frisch-method ranges between 100 μm and 250 μm whereas the radii derived after *O'Connor et al.* [2004] range between 30 μm and 70 μm.

To summarize the results of the retrieval methods of Frisch and O'Connor, it can be concluded that the profiles of LWC and mean radius basically show similar vertical structures. The liquid water content obtained with the O'Connor-method is constantly larger than the respective values obtained with the Frisch-method. The opposite is the case for the mean radius that is larger for the Frisch-method. As a consequence of the Ceilometer- and radar-based approach of O'Connor, no drizzle microphysical properties are derived from within cloud layers. Nevertheless, drizzle formation starts already within the cloud layer. Processes leading to drizzle formation can therefore not be studies with the O'Connor-method. The dependence of the Frisch-method on the assumption that the radar-measured terminal velocity of the drizzle droplets is also their fall velocity is a flaw of that method. Frequently, vertical air motions occur within clouds, affecting the measurement of droplet fall velocity and thus the determination of the drizzle droplet radius after Equation 5.37 The following Chapter 7 addresses this issue more detailed.

7 Correction of drizzle terminal velocity for vertical air motions

In Chapters 4 and 5 it was already discussed that a direct relationship between measured Doppler spectrum and the corresponding droplet size distribution can only be established when atmospheric air motions are absent. All applications of the Frisch-method in the previous Chapter 6 rely on that assumption. As it can be seen in the various case studies presented in this work (e.g., Section 3.5), convective vertical air motions continuously occur in all observed clouds. Otherwise Doppler spectra of drizzling clouds would look similar to the theoretical one shown in Section 4.3.2. As is however obvious from the case study presented in Section 3.5, also upward motions are observed within clouds and even within precipitation. The actual fall velocity v_f is the residual of the vertical velocity of air v_air substracted from the measured Doppler velocity v_d:

$$v_\mathrm{f} = v_\mathrm{d} - v_\mathrm{air} \tag{7.54}$$

Thus, Equation 7.54 shows that if a downdraft occurs ($v_\mathrm{air} < 0$), the Doppler velocity, i.e., the terminal velocity, increases and vice versa. Please note that also the fall velocity v_f is negative in case of a downward motion.

An approach to overcome the uncertainty caused by air motions would be to measure v_air in order to derive the actual fall velocity v_f after Equation 7.54. This could be possible from Doppler lidar measurements. In Section 5.3 and also in the description of Figure 2 it was explained that lidar is much more sensitive to a large number of small droplets than to a small number of large droplets. As was also shown, the opposite is the case for radar. Thus even within precipitation, Doppler lidar can be able to measure the motion of the much larger number of aerosol particles or cloud droplets. The movement of these targets is determined by the air motion.

In Section 7.1 the case study that was already introduced in Section 6.3 is extended by Doppler lidar measurements and a first attempt to check for the applicability of a correction method for drizzle fall speed is presented.

7.1 Vertical-velocity correction for a drizzling cloud

Figure 29 shows the vertical-velocity measurements of the TROPOS Doppler lidar Wili (Figure 29 (a)) and of MIRA-35 (Figure 29 (c)) for the same time period as for the radar measurement presented in Section 6.3. It can be seen that the WiLi-measurement only detected the vertical velocity at the base of the actual cloud layer, as a comparison with the ceilometer measurement in Figure 26 shows. Up-

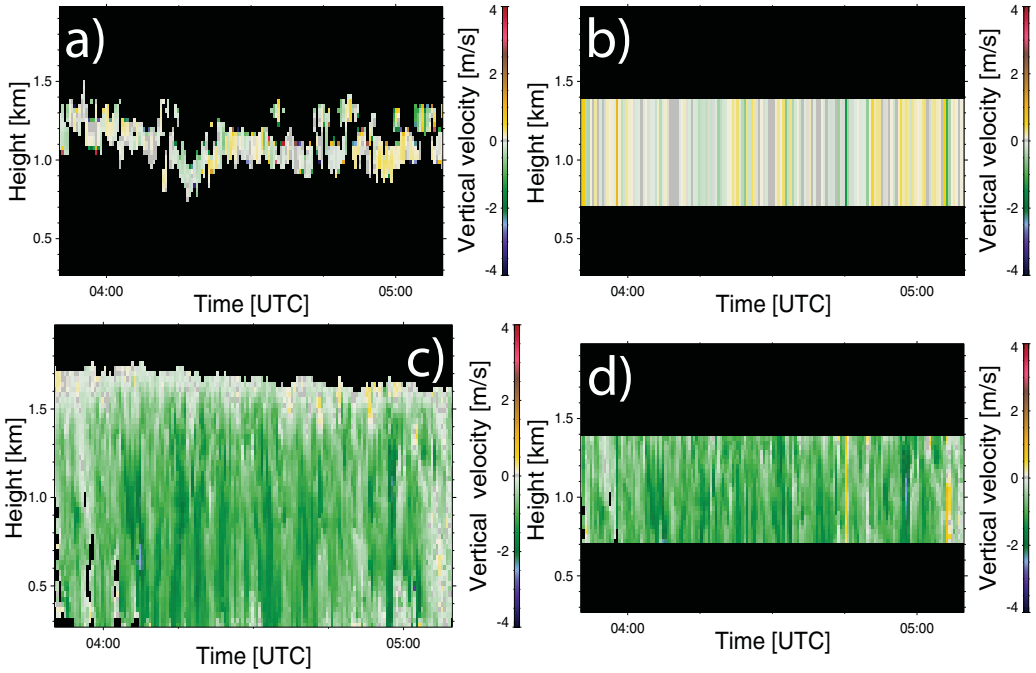

Figure 29: Scheme of the vertical-velocity correction for the drizzling stratus case observed on 10 September 2011 that was introduced in Section 6.3. (a) shows the Doppler velocity observed with WiLi, (b) shows the extrapolated vertical velocities of WiLi used for the velocity correction, (c) shows the Doppler velocity measured with MIRA-35 before the vertical-velocity correction, and (d) shows Doppler velocity of MIRA-35 after the correction.

and downdrafts occurred alternatingly in a range of v_{air} from $-1\ \mathrm{m\,s^{-1}}$ to $+1\ \mathrm{m\,s^{-1}}$. Assuming that Equation 7.54 is valid, i.e., v_{f} is the difference between $v_{\mathrm{d}} - v_{\mathrm{air}}$, a large impact on the retrieved drizzle microphysics is likely when the velocity-correction is applied to the Frisch-method.

In order to apply the velocity correction it is assumed that v_{air} measured at the cloud base is valid over a specific vertical range. In that case it was assumed that this range is between 700 m and 1400 m. The velocity value of every profile that was used was the second one above cloud base. In the first velocity gate at cloud base, the signal detected with WiLi is subject to measurement noise. In addition, the vertical velocity must be smoothed to the temporal resolution of the radar measurement of 30 s. By this method the effect of small-scale turbulences on the WiLi-measurement is removed. Small-scale turbulences are not captured with MIRA-35, because the sample volume is too large (see Figure 5 and, e.g., a discussion in *O'Connor et al.* [2004]).

The time-height cross-section of v_{air} that was used for the correction of v_{d} is shown in Figure 29 (b). Again the alternating up- and downdrafts can be seen. The original radar measurement of v_{d} is shown in Figure 29 (c) and the corrected fall velocity v_{f} can be seen in Figure 29 (d).

7.2 Microphysical properties of a drizzling stratus after vertical-velocity correction

With the corrected values of the fall velocity the microphysical properties of drizzle droplets are calculated again with the Frisch-method. The remaining radar-measured input parameters σ_d and Z that determine the microphysical drizzle properties were not corrected and are the same as in Section 6.3.

The mean radius, liquid water content, and the droplet number concentration for the corrected fall velocity were calculated for the height range from 700 to 1400 m. Figure 30 shows the results of the calculation. First, in Figure 30 (a) the preprocessed vertical velocity is shown. The coloured curves in Figure 30 display droplet number concentration, droplet mean radius, and liquid water content, respectively for the same four time points as the ones in Figures 27.

The radar-measured vertical velocity v_d at the four time points was corrected by $v_{air} = +0.13\ \mathrm{m\,s^{-1}}$ for the black profile (4:07:44 UTC), by $v_{air} = -0.44\ \mathrm{m\,s^{-1}}$ for the red profile (4:18:45 UTC), by $v_{air} = -0.07\ \mathrm{m\,s^{-1}}$ for the green one (4:38:45 UTC),

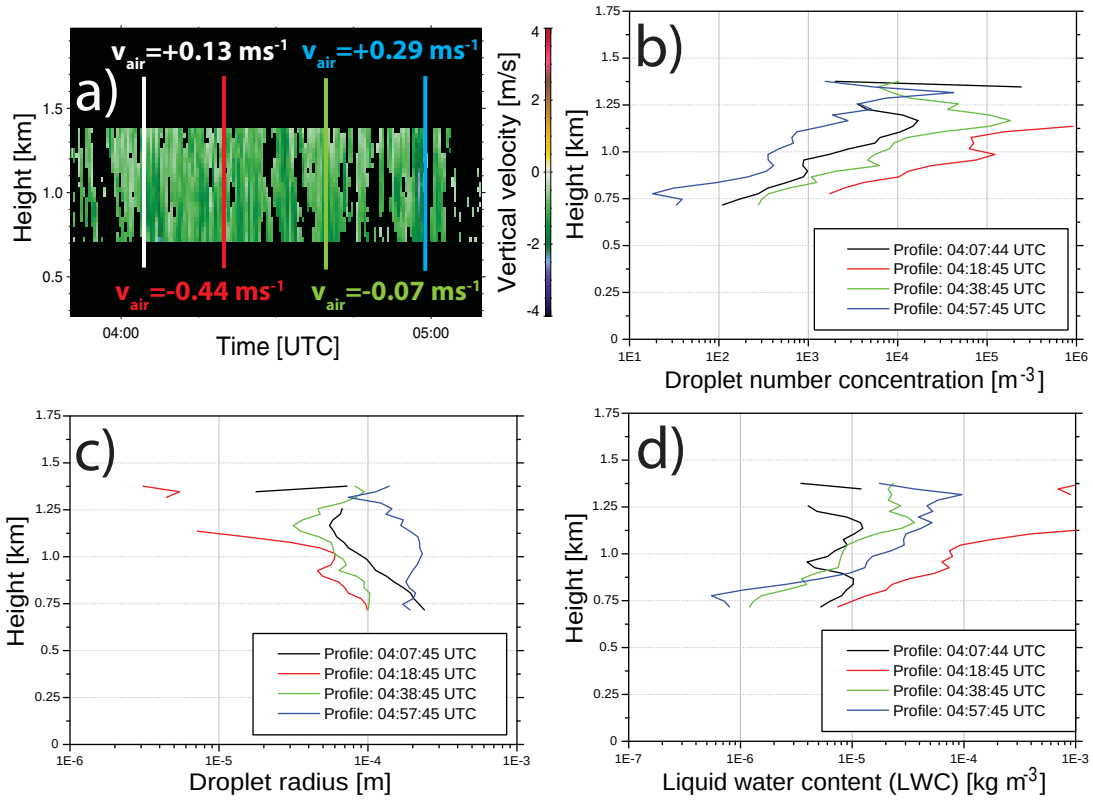

Figure 30: Microphysical drizzle properties obtained with the Frisch-method with corrected vertical velocities for four time points during the observation of a drizzling stratus cloud on 10 September 2011 that was introduced in Figure 26. (a) shows the corrected and preprocessed Doppler velocity measured with MIRA-35 (b) shows the droplet number concentration, (c) shows the mean droplet radius, and (d) shows the liquid water content.

and by $v_{\mathrm{air}} = +0.29\ \mathrm{m\,s^{-1}}$ for the blue profile (4:57:45 UTC). A correction for a downdraft $v_{\mathrm{air}} < 0\ \mathrm{m\,s^{-1}}$ increases v_{f} (i.e., the droplet falls slower), a correction with an updraft the decreases v_{f} (i.e., the droplet falls faster).

In Figure 30 (b) the droplet number concentration is illustrated. It can be seen that the profiles span over a wider range of droplet number as the uncorrected profiles in Figure 27 (b). After correction with $v_{\mathrm{air}} < 0\ \mathrm{m\,s^{-1}}$ (downdrafts) the droplet number concentration increases. For $v_{\mathrm{air}} > 0\ \mathrm{m\,s^{-1}}$ (updrafts) the number concentration decreases, respectively.

The profiles of the mean droplet radius are illustrated in Figure 30 (c). In comparison to the velocity-uncorrected profiles of the mean droplet radius in Figure 27 (a) it can be seen that the velocity-corrected profiles span also over a larger range. The profiles that were corrected for downdrafts are shifted to smaller droplet radii and the ones that were corrected for updrafts show larger mean droplet radii. In comparison to the mean-radius profiles obtained with the O'Connor-method (Figure 27 (b)) it can be seen that the ones that were corrected for an updraft (black and blue curves) agree better to the respective ones of *O'Connor et al.* [2005].

In Figure 30 (d) the liquid water content is illustrated. Compared to the velocity-uncorrected profiles in Figure 27 (c) it can be seen that the downdraft-correction increases the LWC. The updraft-correction leads to lower liquid water contents. The LWC-profiles that were corrected for downdrafts fit better to the results obtained after *O'Connor et al.* [2005] shown in Figure 27 (d).

In conclusion it must be stated that the effect of the vertical-velocity correction is inconclusive. In comparison to the method of *O'Connor et al.* [2005] no improvements were derived. Whereas the mean radius agreed better after correction for atmospheric updrafts, the opposite was the case for the retrieval of the drizzle liquid water content. Further remarks on possible improvements of the vertical-velocity correction are given in the conclusions presented in the following Chapter 8.

8 Summary and conclusions

In the scope of this thesis measurements of a vertically pointing cloud radar were used to derive microphysical properties of drizzle. The data analysis was based on the measurement of the fraction and the Doppler shift of radiation that is backscattered to the radar by clouds and drizzle droplets. In Chapter 2 the theoretical background of the cloud-radar principle was given that explained the relationship between a droplet size distribution and the radar signal. It was described that the detected radar signal is a function of the droplet number and the sixth power of the droplet diameter. Further it was shown that measuring the Doppler spectra is necessary for the determination of a droplet size distribution.

The Doppler velocity is related to the droplet radius. In a measurement example of 27 December 2011 illustrated in Figure 16 it was demonstrated that it is possible to derive information about the droplet size distribution from the Doppler spectrum. The shape, the size range, and the expected number of modes of the droplet size distribution can be assumed from the measurement.

Simulation studies have shown that the Doppler spectrum can be calculated from a given droplet size distribution by an approximation of the relationship between radius and fall velocity of the hydrometeors. The simulations illustrate the shape of the Doppler spectrum and its relationship to the assumed droplet size distribution.

To determine microphysical properties of drizzle droplets in this study two methods were used. The first method was provided by *Frisch et al.* [1995]. The determination of microphysical properties of drizzle and cloud droplets is based on solving a logarithmic normal distribution. The three unknown parameters of total number concentration, logarithmic width, and mean radius needed to describe the size distribution of the drizzle droplets can be calculated from the radar data. The only assumption that needs to be made is an approximation of the relationship between fall velocity and droplet radius. The velocity range of this approximation is valid for the drizzle droplet size range. Large discrepancies were found between different parametrizations of the relationship between droplet radius and fall velocity. The separation of cloud and drizzle droplets was additionally done by setting a threshold for the radar-measured reflectivity. So the data had to be preprocessed before the microphysical properties of the drizzle droplets could be calculated.

Case studies of the microphysical property determination of drizzle droplets were presented in Sections 6.2 and 6.3. In the scope of the second case study the results were compared to the ones of a method provided by *O'Connor et al.* [2005]. This method is based on combined measurements of lidar and cloud radar to calculate parameters that solve a normalized Gamma-distribution. In turn, no information on the Doppler velocity and thus no assumption of a relationship between droplet radius and fall velocity must be made. In comparison to the Frisch-method the

O'Connor-method separates drizzle from cloud droplets via the lidar-detected signal. The backscatter efficiency of the lidar increases rapidly when cloud droplets are present. The relationship between droplet size and backscatter efficiency for typical wavelengths used by cloud radar and lidar was explained in Section 2.1 and illustrated in Figure 1.

The results of the methods of Frisch and O'Connor were found to differ significantly (see Figure 28). Mean droplet radii determined with the Frisch-method were one to two orders of magnitude lower than the ones obtained with the method of *O'Connor et al.* [2005]. In turn, the Frisch-method yielded liquid water contents that are about a factor of two to four larger than the corresponding ones derived after *O'Connor et al.* [2005].

The Frisch-method is based on the assumption that the observed Doppler velocity is a direct measure of the fall velocity of the droplets. It was however shown that the Doppler velocity is the sum of the fall velocity and the vertical air motion. To estimate the influence of vertical air motions on the calculated microphysical drizzle droplet properties the Doppler velocity measured with radar was corrected for the vertical air motion measured with a Doppler lidar.

Recalculation of the microphysical drizzle properties with the velocity-corrected data show large differences in comparison to the results without velocity correction (see Figure 29). When the velocity is corrected for an updraft the mean droplet radius increases, whereas liquid water content and the droplet number concentration decreases. For a downdraft-correction the opposite behaviour was observed. The results correspond to the assumed results because the Doppler spectral width was not corrected for the recalculation. A comparison to the results obtained with the method of *O'Connor et al.* [2005] showed that agreement between the two methods did not improve after the vertical-velocity correction. Profiles that were corrected for downdrafts yield a better agreement between the retrieved drizzle liquid water content. In turn, the agreement between the derived mean droplet radii was improved for the profiles that were corrected for updrafts.

Frisch et al. [1995] also provide an approach to derive microphysical properties of cloud droplets. In an example it was however illustrated that this method does not seem to be applicable to ambient clouds.

In future more case studies need to be done in order to estimate the accuracy of the methods provided by *Frisch et al.* [1995] and by *O'Connor et al.* [2004] as well as the determination of microphysical drizzle properties after velocity correction. Due to the lack of validating in-situ measurements no conclusion can to date be drawn about the accuracy of every single method.

Further, the correction of the radar-measured Doppler spectrum by observations of the Doppler lidar should be investigated more detailed. The width of the Doppler spectrum is influenced by atmospheric turbulence. The spectral width increases

when turbulence in the sample volume of the radar is large. Doppler lidars feature fast measurement times on the order of 1 s and a much smaller sample volume. This may allow to use such measurements to correct the Doppler spectrum measured with radar.

The Doppler spectrum could also be used to separate drizzle from cloud droplets in the Frisch-method. As it was shown in the measurement example in Figure 16 the cloud mode and the drizzle mode can be identified in the Doppler spectra. After such a separation, the Frisch-method may provide more-accurate results of drizzle properties from within clouds. This would be an advantage of the Frisch-method in comparison to the O'Connor-method which does not allow the determination of drizzle microphysical properties within clouds.

Bibliography

Ackerman, A. S., O. B. Toon, D. E. Stevens, A. J. Heymsfield, V. Ramanathan, and E. J. Welton (2000), Reduction of tropical cloudiness by soot, *Science*, *288*, 1042-1047, doi:10.1126/science.288.5468.1042.

Albrecht, B. A. (1989), Aerosols, cloud microphysics, and fractional cloudiness, *Science*, *245*, 1227-1230, doi:10.1126/science.245.4923.1227.

Althausen, D., R. Engelmann, H. Baars, B. Heese, A. Ansmann, D. Müller, and M. Komppula (2009), Portable raman lidar Polly^{XT} for automated profiling of aerosol backscatter, extinction, and depolarization, *Journal of Atmospheric and Oceanic Technology*, *26*, 2366, doi:10.1175/2009JTECHA1304.1.

Ansmann, A., I. Mattis, D. Müller, U. Wandinger, M. Radlach, D. Althausen, and R. Damoah (2005), Ice formation in Saharan dust over central Europe observed with temperature/humidity/aerosol Raman lidar, *Journal of Geophysical Research*, *110*, D18S12, doi:10.1029/2004JD005000.

Atlas, D., R. C. Srivastava, and R. S. Sekhon (1973), Doppler radar characteristics of precipitation at vertical incidence, *Reviews of Geophysics and Space Physics*, *11*, 1, doi:10.1029/RG011i001p00001.

Beard, K. V. (1985), Simple altitude adjustments to raindrop velocities for doppler radar analysis, *Journal of Atmospheric and Oceanic Technology*, *2*, 468–471, doi:10.1175/1520-0426(1985)002<0468:SAATRV>2.0.CO;2.

Bohren, C. F., and D. R. Huffman (1983), *Absorption and scattering of light by small particles*, 530 pp., John Wiley.

Crewell, S., U. Löhnert, M. Mech, and C. Simmer (2010), Mikrowellenradiometrie für Wassserdampf- und Wolkenbeobachtungen, in *promet*, vol. 36, edited by J. Rapp, chap. 4, pp. 109–118, Deutscher Wetterdienst.

Davidson, K. L., C. W. Fairall, P. Jones Boyle, and G. E. Schacher (1984), Verification of an atmospheric mixed-layer model for a coastal region, *Journal of Applied Meteorology*, *23*, 617-636, doi:10.1175/1520-0450(1984)023<0617:VOAAML>2.0.CO;2.

Deirmendjian, D. (1969), *Electromagnetic scattering on spherical polydispersions*, 318 pp., RAND Corporation.

Deirmendjian, D. (1975), Far-infrared and submillimeter wave attenuation by clouds and rain, *Journal of Applied Meteorology*, *14*, 1584-1593, doi:10.1175/1520-0450(1975)014<1584:FIASWA>2.0.CO;2.

Ditas, F., R. A. Shaw, H. Siebert, M. Simmel, B. Wehner, and A. Wiedensohler (2012), Aerosols-cloud microphysics-thermodynamics-turbulence: evaluating supersaturation in a marine stratocumulus cloud, *Atmospheric Chemistry & Physics*, *12*, 2459-2468, doi:10.5194/acp-12-2459-2012.

Engelmann, R. (2009), Aerosol vertical exchange in the convective planetary boundary layer — turbulent particle flux measurements with combined wind and aerosol lidar, Ph.D. thesis, University of Leipzig.

Engelmann, R., U. Wandinger, A. Ansmann, D. Müller, E. Zeromskis, D. Althausen, and B. Wehner (2008), Lidar observations of the vertikal aerosol flux in the planetary boundary layer, pp. 1296–1306, American Meteorological Society, doi: 10.1175/2007JTECHA967.1.

Feingold, G., W. L. Eberhard, D. E. Veron, and M. Previdi (2003), First measurements of the Twomey indirect effect using ground-based remote sensors, *Geophysical Research Letters*, *30*(6), 1287, doi:10.1029/2002GL016633.

Frisch, A. S., C. W. Fairall, and J. B. Snider (1995), Measurement of stratus cloud and drizzle parameters in ASTEX with a K_α-band doppler radar and a microwave radiometer, *Journal of Atmospheric Sciences*, *52*, 2788-2799, doi: 10.1175/1520-0469(1995)052<2788:MOSCAD>2.0.CO;2.

Frisch, A. S., G. Feingold, C. W. Fairall, T. Uttal, and J. B. Snider (1998), On cloud radar and microwave radiometer measurements of stratus cloud liquid water profiles, *Journal of Geophysical Research*, *103*, 23195-23198, doi:10.1029/98JD01827.

Görsdorf, U. (2009), Cloud Radar, in *Integrated Ground-Based Remote-Sensing Stations for Atmospheric Profiling*, vol. 1, edited by D. A. M. Engelbart, W. A. Monna, J. Nash, and C. Mätzler, chap. 7, p. 380, European Communities, doi: 10.2831/10752.

Gossard, E. E., R. O. Strauch, and R. R. Rogers (1990), Evolution of dropsize distributions in liquid precipitation observed by ground-based doppler radar, *Journal of Atmospheric and Oceanic Technology*, *7*, 815-828, doi:10.1175/1520-0426(1990)007<0815:EODDIL>2.0.CO;2.

Gunn, K. L. S., and T. W. R. East (1954), The microwave properties of precipitation particles, *Quarterly Journal of the Royal Meteorological Society*, *80*(346), 522–545, doi:10.1002/qj.49708034603.

Hansen, J. E., and L. D. Travis (1974), Light scattering in planetary atmospheres, *Space Science Reviews*, *16*, 527-610, doi:10.1007/BF00168069.

Hayasaka, T., N. Kikuchi, and M. Tanaka (1995), Absorption of solar radiation by stratocumulus clouds: Aircraft measurements and theoretical calculations, *Journal of Applied Meteorology*, *34*, 1047-1055, doi:10.1175/1520-0450(1995)034<1047:AOSRBS>2.0.CO;2.

Heintzenberg, J., and R. J. Charlson (2009), *Clouds in the perturbed climate system*, 576 pp., MIT Press, Cambridge, MA, USA.

Holben, B. N., T. F. Eck, I. Slutsker, J. Tanre, J. P. Buis, A. Stezer, E. Vermote, J. A. Reagan, Y. J. Kaufman, T. Kakajima, F. Lavenu, I. Jankowiak, and A. Smirnov (1998), AERONET — A federated instrument network and data archive for aerosol characterization, *66*, 1-16.

Illingworth, A. J., R. J. Hogan, E. J. O'Connor, D. Bouniol, M. E. Brooks, J. Delanoë, D. P. Donovan, J. D. Eastment, N. Gaussiat, J. W. F. Goddard, M. Haeffelin, H. K. Baltink, O. A. Krasnov, J. Pelon, J.-M. Piriou, A. Protat, H. W. J. Russchenberg, A. Seifert, A. M. Tompkins, G.-J. van Zadelhoff, F. Vinit, U. Willén, D. R. Wilson, and C. L. Wrench (2007), Cloudnet, *Bulletin of the American Meteorological Society*, *88*, 883, doi:10.1175/BAMS-88-6-883.

Intrieri, J. M., G. L. Stephens, W. L. Eberhard, and T. Uttal (1993), A method for determining cirrus cloud particle sizes using lidar and radar backscatter technique, *Journal of Applied Meteorology*, *32*, 1074-1082, doi:10.1175/1520-0450(1993)032<1074:AMFDCC>2.0.CO;2.

Jaffrain, J., A. Studzinski, and A. Berne (2011), A network of disdrometers to quantify the small-scale variability of the raindrop size distribution, *Water Resources Research*, *47*, W00H06, doi:10.1029/2010WR009872.

Kraus, H. (2000), *Die Atmosphäre — Eine Einführung in die Meteorologie*, 3rd ed., 422 pp., Springer Verlag.

Löhnert, U., and S. Crewell (2003), Accuracy of cloud liquid water path from ground-based microwave radiometry — 1: Dependency on cloud model statistics, *Radio Science*, *38*(3), 8041, doi:10.1029/2002RS002654.

Martin, G. M., D. W. Johnson, and A. Spice (1994), The measurement and parameterization of effective radius of droplets in warm stratocumulus clouds, *Journal of Atmospheric Sciences*, *51*, 1823-1842, doi:10.1175/1520-0469(1994)051<1823:TMAPOE>2.0.CO;2.

Mattis, I., A. Ansmann, D. Althausen, V. Jaenisch, U. Wandinger, D. Müller, Y. F. Arshinov, S. M. Bobrovnikov, and I. B. Serikov (2002), Relative-humidity profiling in the troposphere with a Raman lidar, *Applied Optics*, *41*, 6451–6462.

Miles, N. L., J. Verlinde, and E. E. Clothiaux (2000), Cloud droplet size distributions in low-level stratiform clouds, *Journal of Atmospheric Sciences*, *57*, 295–311, doi: 10.1175/1520-0469(2000)057<0295:CDSDIL>2.0.CO;2.

Montopoli, M., and F. M. Mazano (2010), Meteorological radar systems, in *Integrated ground-based observing systems*, edited by D. Cimini, F. M. Marzano, and G. Visconti, 1. Auflage, chap. I.2, pp. 33–57, Springer Heidelberg Dordrecht London New York, doi:10.1007/978-3-642-12968-1_2.

O'Connor, E. J., A. J. Illingworth, and R. J. Hogan (2004), A technique for autocalibration of cloud lidar, *Journal of Atmospheric and Oceanic Technology*, *21*, 777, doi:10.1175/1520-0426(2004)021<0777:ATFAOC>2.0.CO;2.

O'Connor, E. J., R. J. Hogan, and A. J. Illingworth (2005), Retrieving stratocumulus drizzle parameters using doppler radar and lidar, *Journal of Applied Meteorology*, *44*, 14-27, doi:10.1175/JAM-2181.1.

Ohmura, A., H. Gilgen, H. Hegner, G. Müller, M. Wild, E. G. Dutton, B. Forgan, C. Fröhlich, R. Philipona, A. Heimo, G. König-Langlo, B. McArthur, R. Pinker, C. H. Whitlock, and K. Dehne (1998), Baseline surface radiation network (BSRN/WCRP): new precision radiometry for climate research, *Bulletin of the American Meteorological Society*, *79*, 2115-2136, doi:10.1175/1520-0477(1998) 079<2115:BSRNBW>2.0.CO;2.

Peters, G., and U. Görsdorf (2010), Wolkenradar — Prinzipien und Messungen, in *promet*, vol. 36, edited by J. Rapp, chap. 4, pp. 144–153, Deutscher Wetterdienst.

Pincus, R., and M. B. Baker (1994), Effect of precipitation on the albedo susceptibility of clouds in the marine boundary layer, *Nature*, *372*, 250-252, doi: 10.1038/372250a0.

Richardson, M. S., P. J. DeMott, S. M. Kreidenweis, D. J. Cziczo, E. J. Dunlea, J. L. Jimenez, D. S. Thomson, L. L. Ashbaugh, R. D. Borys, D. L. Westphal, G. S. Casuccio, and T. L. Lersch (2007), Measurements of heterogeneous ice nuclei in the western United States in springtime and their relation to aerosol characteristics, *Journal of Geophysical Research*, *112*, D02209, doi:10.1029/2006JD007500.

Rinehart, R. E. (1997), *Radar for Meteorologists*, 2, 428 pp., Rinehart Publishing.

Rose, T., S. Crewell, U. Löhnert, and C. Simmer (2005), A network-suitable microwave radiometer for operational monitoring of the cloudy atmosphere, *Atmospheric Research*, *75*, 183-200, doi:10.1016/j.atmosres.2004.12.005.

Russell, R. W., and J. W. Wilson (1996), Aerial plankton detected by radar, *Nature 381, 200-201*, *381*, 200-201, doi:10.1038/381200a0.

Seifert, P., A. Ansmann, I. Mattis, U. Wandinger, M. Tesche, R. Engelmann, D. Müller, C. Pérez, and K. Haustein (2010), Saharan dust and heterogeneous ice formation: Eleven years of cloud observations at a central European EARLINET site, *Journal of Geophysical Research (Atmospheres)*, *115*, D20201, doi: 10.1029/2009JD013222.

Shettle, E. P. (1990), Models of aerosols, clouds, and precipitation for atmospheric propagation studies, in *AGARD, Atmospheric Propagation in the UV, Visible, IR, and MM-Wave Region and Related Systems Aspects 14 p (SEE N90-21907 15-32)*, edited by E. P. Shettle.

Slingo, A., R. Brown, and C. L. Wrench (1982), A field study of nocturnal stratocumulus — III: High resolution radiative and microphysical observations, *Quarterly Journal of the Royal Meteorological Society*, *108*, 145-165, doi:10.1002/qj.49710845509.

Solomon, S., D. Qin, M. Manning, Z. Chen, M. Marquis, K. B. Averyt, M. Tignor, and H. L. Miller (Eds.) (2007), *Contribution of Working Group I to the Fourth Assessment Report of the Intergovernmental Panel on Climate Change*, Cambridge University Press, Cambridge, United Kingdom and New York, NY, USA.

Szyrmer, W., and I. Zawadzki (1999), Modeling of the melting layer. Part I: Dynamics and microphysics, *Journal of Atmospheric Sciences*, *56*, 3573-3592, doi: 10.1175/1520-0469(1999)056<3573:MOTMLP>2.0.CO;2.

Twomey, S. (1977), The influence of pollution on the shortwave albedo of clouds., *Journal of Atmospheric Sciences*, *34*, 1149-1154, doi:10.1175/1520-0469(1977)034<1149:TIOPOT>2.0.CO;2.

Van de Hulst, H. C. (1957), *Light scattering by small particles*, 470 pp., John Wiley & Sons, Ltd.

Van Zanten, M. C., B. Stevens, G. Vali, and D. H. Lenschow (2005), Observations of drizzle in nocturnal marine stratocumulus, *Journal of Atmospheric Sciences*, *62*, 88–106, doi:10.1175/JAS-3355.1.

Weitkamp, C. (2005), *Lidar, Range-resolved optical remote sensing of the atmosphere*, 456 pp., Springer, Berlin.

Wiegner, M., and A. Geiß (2012), Aerosol profiling with the Jenoptik ceilometer CHM15kx, *Atmospheric Measurement Techniques*, *5*, 1953-1964, doi:10.5194/amt-5-1953-2012.

Eidesstattliche Erklärung

Hiermit erkläre ich, dass ich die Masterarbeit selbständig verfasst habe und keine anderen als die angegebenen Quellen und Hilfsmittel benutzt habe. Alle Stellen der Arbeit, die wörtlich oder sinngemäß aus Veröffentlichungen oder aus anderweitigen fremden Äußerungen entnommen wurden, sind als solche kenntlich gemacht. Ferner erkläre ich, dass die Arbeit noch nicht in einem anderen Studiengang als Prüfungsleistung verwendet wurde.

Leipzig, den .2012

Einverständniserklärung zur Veröffentlichung der Arbeit in der Universitätsbibliothek

Ich bin einverstanden, dass diese Arbeit nach positiver Begutachtung in der Universitätsbibliothek zur Verfügung steht.

Leipzig, den .2012